

Magnetic fields on young, moderately rotating Sun-like stars – I. HD 35296 and HD 29615

I. A. Waite,^{1★} S. C. Marsden,¹ B. D. Carter,¹ P. Petit,^{2,3} J.-F. Donati,^{2,3} S. V. Jeffers⁴ and S. Boro Saikia⁴

¹Computational Engineering and Science Research Centre, University of Southern Queensland, Toowoomba, QLD 4350, Australia

²Institut de Recherche en Astrophysique et Planétologie, Université de Toulouse, UPS-OMP, F-31400 Toulouse, France

³CNRS, Institut de Recherche en Astrophysique et Planétologie, 14 Avenue Edouard, Belin, F-31400 Toulouse, France

⁴Institut für Astrophysik, Georg-August-Universität Göttingen, Friedrich-Hund-Platz 1, D-37077 Göttingen, Germany

Accepted 2014 December 31. Received 2014 December 31; in original form 2014 April 20

ABSTRACT

Observations of the magnetic fields of young solar-type stars provide a way to investigate the signatures of their magnetic activity and dynamos. Spectropolarimetry enables the study of these stellar magnetic fields and was thus employed at the T lescope Bernard Lyot and the Anglo-Australian Telescope to investigate two moderately rotating young Sun-like stars, namely HD 35296 (V119 Tau, HIP 25278) and HD 29615 (HIP 21632). The results indicate that both stars display rotational variation in chromospheric indices consistent with their spot activity, with variations indicating a probable long-term cyclic period for HD 35296. Additionally, both stars have complex, and evolving, large-scale surface magnetic fields with a significant toroidal component. High levels of surface differential rotation were measured for both stars. For the F8V star HD 35296 a rotational shear of $\Delta\Omega = 0.22^{+0.04}_{-0.02}$ rad d⁻¹ was derived from the observed magnetic profiles. For the G3V star HD 29615, the magnetic features indicate a rotational shear of $\Delta\Omega = 0.48^{+0.11}_{-0.12}$ rad d⁻¹, while the spot features, with a distinctive polar spot, provide a much lower value of $\Delta\Omega$ of $0.07^{+0.10}_{-0.03}$ rad d⁻¹. Such a significant discrepancy in shear values between spot and magnetic features for HD 29615 is an extreme example of the variation observed for other lower mass stars. From the extensive and persistent azimuthal field observed for both targets, it is concluded that a distributed dynamo operates in these moderately rotating Sun-like stars, in marked contrast to the Sun’s interface-layer dynamo.

Key words: line: profiles – stars: activity – stars: individual: HD 35296 – stars: individual: HD 29615 – stars: magnetic field – stars: solar-type – starspots.

1 INTRODUCTION

Observations of the distribution of magnetic fields offer insights into how magnetic dynamos are governed by physical properties such as mass, rotation and age, with younger Sun-like stars providing proxies for understanding the history of the Sun’s activity and dynamo. Today we can readily observe the starspots and surface magnetic fields of young Sun-like stars, to reconstruct their surface magnetic topologies and differential rotation. Multi-epoch observations of stellar magnetic regions also offer the prospect of revealing how magnetic activity cycles can emerge in stars like the Sun. Such observations can allow us to study the relative role of two possible dynamo theories, namely the widely accepted Sun’s

‘shell’ dynamo that operates at the interface layer between the radiation and convection zone and the ‘distributed’ dynamo thought to be operating in young, active stars where the dynamo is present throughout the convection zone (e.g. Brandenburg et al. 1989; Moss et al. 1995; Donati et al. 2003a; Brown et al. 2010). While the large-scale toroidal magnetic field is understood to be buried deep inside the Sun, it has been observed on a range of rapidly rotating solar-type stars through the presence of strong unipolar surface azimuthal magnetic fields (e.g. Donati et al. 2003a; Petit et al. 2004a; Marsden et al. 2006). Petit et al. (2008) concluded that the rotation period threshold where the surface toroidal field begins to dominate over the poloidal field is ≈ 12 d. Thus, rotation plays an important role in the generation of the magnetic field and the complexity of these fields.

The study of these complex magnetic fields on Sun-like stars has been greatly advanced using the technique of Zeeman–Doppler

*E-mail: waite@usq.edu.au

imaging (ZDI; Semel 1989; Donati & Semel 1990; Donati & Brown 1997; Donati et al. 2003a). ZDI has been performed for a small sample of single, rapidly rotating early G-type stars such as HD 171488 (V889 Her; SpType: G2V; Marsden et al. 2006; Jeffers & Donati 2008; Jeffers et al. 2011) and HD 141943 (SpType: G2; Marsden et al. 2011a,b). Differential rotation, given its likely importance to the operation of the dynamo, is a key measurement. These stars have shown significant levels of differential rotation using both brightness and magnetic features. Jeffers & Donati (2008) observed HD 171488 and measured $\Delta\Omega = 0.52 \pm 0.04 \text{ rad d}^{-1}$ using spot features while $\Delta\Omega = 0.47 \pm 0.04 \text{ rad d}^{-1}$ was measured using magnetic features. Jeffers et al. (2011) in their more recent study measured slightly lower values of $\Delta\Omega \sim 0.4 \text{ rad d}^{-1}$ (Stokes *I*) and $\sim 0.415\text{--}0.45 \text{ rad d}^{-1}$ (Stokes *V*). These levels of differential rotation are similar to an earlier study by Marsden et al. (2006) of $\Delta\Omega = 0.402 \pm 0.044 \text{ rad d}^{-1}$ (using spot features). Marsden et al. (2011b) observed HD 141943 and measured $\Delta\Omega = 0.24 \pm 0.03 \text{ rad d}^{-1}$ using spot features with $\Delta\Omega = 0.45 \pm 0.08 \text{ rad d}^{-1}$ using magnetic features on their 2010 data set (and slightly lower with $\Delta\Omega = 0.36 \pm 0.09 \text{ rad d}^{-1}$ for their 2007 data). Conversely, slowly rotating stars such as HD 190771 (SpType: G2V), with a $v\sin i$ of $4.3 \pm 0.5 \text{ km s}^{-1}$, also exhibit measurable differential rotation with $\Delta\Omega = 0.12 \pm 0.03 \text{ rad d}^{-1}$ using magnetic features (Petit et al. 2008). In addition to relatively high levels of differential rotation, all three stars exhibited complex magnetic topologies with large-scale poloidal and toroidal fields, each with significant higher order components beyond simple dipole fields.

Barnes et al. (2005) first reported the link between differential rotation and effective temperature, and consequently convective turnover time. They were able to develop a correlation between rotational shear and effective temperature for a small sample of stars and determined that as a star's effective temperature increases so does the rotational shear, a trend consistent with the recent theoretical calculations by Kitchatinov & Olemskoy (2011). Additionally, a steep rise in differential rotation for late F-/early G-type stars appears related to the rapid shallowing of the convection zone (e.g. Marsden et al. 2011b). Küker, Rüdiger & Kitchatinov (2011) demonstrate that the extreme levels of rotational shear observed for stars such as HD 171488 can only be explained with a shallow convection zone. Thus, the depth of the convection zone must have a major role in the rotational profile of a solar-type star.

In this study, two moderately rotating, young Sun-like stars were selected based on their similar rotational velocities and sizes, enabling comparisons of their magnetic fields and differential rotations. HD 35296 (SpType: F8V) is a $1.06^{+0.06}_{-0.05} M_{\odot}$ (Holmberg, Nordström & Anderson 2009) star with an estimated photospheric temperature 6170 K (Casagrande et al. 2011) while HD 29615 (SpType: G3V) is a $0.95 M_{\odot}$, $1.0 R_{\odot}$ star (Allende Prieto & Lambert 1999). HD 35296 has a $v\sin i$ of 15.9 km s^{-1} (Ammler-von Eiff & Reiners 2012) while HD 29615 has a $v\sin i$ of $\sim 18 \text{ km s}^{-1}$ (Waite et al. 2011a). The aim is to map the surfaces of these two stars with a view to measuring the rotational shear and magnetic field structures. This will enable further comparisons with stars of similar mass but different rotational velocities. This is Paper I of two papers focusing on the complex nature of the magnetic field topologies of young moderately rotating Sun-like stars as proxies for the evolution of the young Sun. Paper II will focus on the infant Sun EK Draconis (Waite et al., in preparation). This paper is part of the BCool¹

collaboration investigating the magnetic activity of low-mass stars (e.g. Marsden et al. 2014).

2 FUNDAMENTAL PARAMETERS OF THE STARS

The fundamental parameters for the two targets, HD 35296 and HD 29615, are shown in Table 1. Some of these parameters such as projected rotational velocity ($v\sin i$), radial velocity and inclination were measured as part of the imaging process, as explained in Section 5, while other parameters have been taken from the literature.

2.1 HD 35296

HD 35296 (V1119 Tau) is an F8V star (Montes et al. 2001). It has a parallax of $69.51 \pm 0.38 \text{ mas}$ (van Leeuwen 2007) giving a distance of $14.39 \pm 0.08 \text{ pc}$. Samus et al. (2009) identified HD 35296 as a BY Draconis-type variable star. The range of age estimates of this star in the literature is quite large, with Holmberg et al. (2009) estimating an age of 3.3 Gyr, with some authors listing this star as young as 20 Myr or as old as 7.5 Gyr (e.g. Barry 1988; Chen et al. 2001). The equivalent width of the Li I 670.78 nm line is $99 \text{ m}\text{\AA}$, correcting for the nearby 670.744 nm Fe I line using the same factor developed by Soderblom et al. (1993a,b). This is consistent with that measured by Takeda & Kawanomoto (2005) of $94.3 \text{ m}\text{\AA}$. Li & Hu (1998) argued that HD 35296 is a member of the Taurus-Auriga star-forming region that may have reached the zero-age main sequence. When placing this star on the theoretical isochrones of Siess, Dufour & Forestini (2000), the age of this star is between 20 and 50 Myr. Hence, it is likely that this star is quite youthful.

2.2 HD 29615

HD 29615 (HIP 21632) is a G3V star (Torres et al. 2006). The *Hipparcos* space mission measured a parallax of $18.27 \pm 1.02 \text{ mas}$ (van Leeuwen 2007), giving a distance of $54.7^{+3.2}_{-2.9} \text{ pc}$. Zuckerman & Song (2004) proposed that HD 29615 was a member of the Tucana/Horologium association indicating an age of $\sim 30 \text{ Myr}$. Waite et al. (2011a) detected a magnetic field on this star, along with a varying emission equivalent width for the H α line in the range from ~ 370 to $\sim 500 \text{ m}\text{\AA}$ demonstrating the presence of a very active, and variable, chromosphere.

3 OBSERVATIONS AND ANALYSIS

HD 35296 was observed at the T lescope Bernard Lyot (TBL, Observatoire Pic du Midi, France) in 2007 January/February and again in 2008 January/February using the high-resolution spectropolarimeter NARVAL. HD 29615 was observed at the Anglo-Australian Telescope (AAT, New South Wales, Australia) in 2009 November/December using the high-resolution spectropolarimeter Semel Polarimeter (SEMPOL). Journals of observations are given in Tables 2 and 3.

3.1 High-resolution spectropolarimetric observations from the TBL

NARVAL is a bench-mounted, cross-dispersed  chelle spectrograph, fibre-fed from a Cassegrain-mounted polarimeter unit and is similar in function to the SEMPOL used at the AAT, which is described in Section 3.2. NARVAL has a mean pixel resolution of

¹ <http://bcool.ast.obs-mip.fr>

Table 1. The parameters used to produce the maximum-entropy image reconstructions of the two targets, including surface differential rotation measurements. Except otherwise indicated, parameters have been determined by this study.

Parameter	HD 35296	HD 29615
Spectral type	F8V ¹	G3V ²
Equatorial period	$3.48 \pm 0.01 \text{ d}^3$	$2.34^{+0.02}_{-0.05} \text{ d}^4$
Inclination angle	$65^\circ \pm 5^\circ$ ⁵	$65^{+5}_{-10}^\circ$
Projected rotational velocity, $v \sin i$	$15.9 \pm 0.1 \text{ km s}^{-1}$	$19.5 \pm 0.1 \text{ km s}^{-1}$
Photospheric temperature, T_{phot}	6170 K ⁶	$5820 \pm 50 \text{ K}^7$
Spot temperature, T_{spot}	–	3920 K ⁸
Radial velocity, v_{rad}	$38.1 \pm 0.1 \text{ km s}^{-1}$	$19.33 \pm 0.1 \text{ km s}^{-1}$
Stellar radius	$1.10 R_{\odot}^9$	$1.0 R_{\odot}^{10}$
Stellar mass	$1.06^{+0.06}_{-0.05} M_{\odot}^9$	$0.95 M_{\odot}^{10}$
Age	30–50 Myr ¹¹	30 Myr ¹²
Convection zone depth ¹¹ $R_*(R_{\odot})$	0.178 (0.201)	0.252 (0.252)
Stokes <i>I</i> : $\Omega_{\text{eq}} \text{rad d}^{-1}$	–	$2.68^{+0.06}_{-0.02}$
Stokes <i>I</i> : $\Delta\Omega \text{rad d}^{-1}$	–	$0.07^{+0.10}_{-0.03}$
Stokes <i>V</i> : $\Omega_{\text{eq}} \text{rad d}^{-1}$	1.804 ± 0.005	$2.74^{+0.02}_{-0.04}$
Stokes <i>V</i> : $\Delta\Omega \text{rad d}^{-1}$	$0.22^{+0.04}_{-0.02}$	$0.48^{+0.11}_{-0.12}$
Epoch of zero phase (MHJD) ¹³	54133.871035 (2007) 54496.094272 (2008)	55165.011060 (2009)

Notes. ¹Montes et al. (2001).

²Torres et al. (2006).

³Using Stokes *V* data.

⁴Using Stokes *I* data.

⁵The inclination angle of HD 35296 was based on the most recent value of $P \sin \theta = 3.9$ calculated by Ammler-von Eiff & Reiners (2012).

⁶Casagrande et al. (2011).

⁷Using the bolometric corrections of Bessell et al. (1998).

⁸Using the relationship between photospheric and spot temperature provided by Berdyugina (2005).

⁹Based on the values found in Holmberg et al. (2009).

¹⁰Allende Prieto & Lambert (1999).

¹¹Determined from the stellar evolution models of Siess et al. (2000).

¹²Zuckerman & Song (2004).

¹³Modified Heliocentric Julian Date (MHJD) = HJD – 24000000.0.

$1.8 \text{ km s}^{-1} \text{ pixel}^{-1}$ with a spectral coverage from ~ 370 to 1048 nm with a resolution of $\sim 65\,000$ spanning 40 grating orders (orders #22 to #61). NARVAL consists of one fixed quarter-wave retarder sandwiched between two rotating half-wave retarders and coupled to a Wollaston beamsplitter (Aurière 2003). Observations in circular polarization (Stokes *V*) consist of a sequence of four exposures. After each of the exposures, the half-wave Fresnel rhomb of the polarimeter is rotated so as to remove any systematic effects due to variations in the optical throughput, CCD inhomogeneities, terrestrial and stellar rotation, temporal variability and instrumental polarization signals from the telescope and the polarimeter (e.g. Semel, Donati & Rees 1993; Carter et al. 1996; Donati et al. 2003a). Initial reduction was completed using the dedicated pipeline reduction software LIBRE-ESPRIT (Échelle Spectra Reduction: an Interactive Tool), which is based on the algorithm developed by Donati et al. (1997). Silvester et al. (2012) proved that NARVAL is a very stable instrument, with resolution and signal-to-noise ratio (SNR) being constant over the four years of data studies from 2006 to 2010.

3.2 High-resolution spectropolarimetric observations from the AAT

High-resolution spectropolarimetric data were obtained from the AAT using the University College of London Échelle Spectrograph (UCLES) and SEMPOL (Semel et al. 1993; Donati et al. 1997, 2003a). The detector used was the deep depletion EEV2 CCD with $2048 \times 4096 \text{ } 13.5 \mu\text{m pixel}^2$. UCLES was used with a 31.6 gr/mm grating covering 46 orders (orders # 84 to # 129). The central wavelength was 522.002 nm with full wavelength coverage from 438 to 681 nm . The dispersion of $\sim 0.004 \text{ } 958 \text{ nm}$ at order # 129 gave a resolution of approximately $71\,000$. The mean resolution for the AAT spectra was determined to be $1.689 \text{ km s}^{-1} \text{ pixel}^{-1}$. The operation of SEMPOL is similar to that explained in Section 3.1. After each exposure, the half-wave Fresnel rhomb is rotated between $+45^\circ$ and -45° so as to remove any systematic effects. Initial reduction was completed using ESPRIT developed for SEMPOL (Donati et al. 1997). SEMPOL is not as efficient as NARVAL; hence, the SNR is lower, even though the AAT is a 3.9 m telescope whereas the TBL is a 2 m telescope. In addition, the spectral range of SEMPOL is

Table 2. Journal of spectropolarimetric observations of HD 35296 using the TBL.

UT date	UT middle	Exp. time ¹ (s)	Mean SNR for Stokes V LSD profiles
2007 Jan 24	21:08:45	1 × 300	– ²
2007 Jan 26	21:10:23	4 × 300	19 762
2007 Jan 27	20:18:17	4 × 600	39 439
2007 Jan 29	19:29:15	4 × 600	38 358
2007 Feb 02	21:17:29	4 × 300	4223
2007 Feb 03	20:15:21	4 × 300	29 940
2007 Feb 04	20:06:35	4 × 300	25 137
2007 Feb 08	20:30:51	4 × 300	25 639
2008 Jan 19	20:01:46	4 × 300	17 208
2008 Jan 20	21:45: 1	4 × 300	20 581
2008 Jan 21	19:42:27	4 × 300	24 563
2008 Jan 21	20:53:24	4 × 200	22 146
2008 Jan 22	20:09:11	4 × 300	21 913
2008 Jan 23	20:10:31	4 × 300	21 825
2008 Jan 24	20:39:32	4 × 300	13 296
2008 Jan 25	20:15:17	4 × 300	19 723
2008 Jan 26	20:14:43	4 × 300	21 148
2008 Jan 27	20:30:50	4 × 300	21 245
2008 Jan 28	21:56:43	4 × 300	21 245
2008 Jan 29	20:50:19	4 × 300	25 946
2008 Feb 02	20:45:15	4 × 300	24 375
2008 Feb 04	20:20:19	4 × 300	27 669
2008 Feb 05	20:21:18	4 × 300	22 909
2008 Feb 06	21:11: 7	4 × 300	25 579
2008 Feb 09	20:34:17	4 × 300	24 555
2008 Feb 10	19:13:58	4 × 300	29 354
2008 Feb 11	20:39:11	4 × 300	25 414
2008 Feb 12	20:45:32	4 × 300	27 269
2008 Feb 13	20:39:30	4 × 300	24 182
2008 Feb 14	21:00: 8	4 × 300	24 386
2008 Feb 15	20:37: 6	4 × 300	28 120

Notes. ¹Each sequence consists of four sub-exposures with each sub-exposure being 300 s (for example).

²Only one Stokes *I* spectrum was taken on this night. The SNR, as measured for order number 41, was 272.

smaller; therefore, there are fewer spectral lines available to extract the magnetic signature from the star's light.

3.3 Spectropolarimetric analysis

Preliminary processing involved subtracting the bias level and using a nightly master flat combining typically 20 flat-field exposures. Each stellar spectrum was extracted and wavelength calibrated against a thorium–argon lamp.

After using LIBRE-ESPRIT (TBL) or ESPRIT (AAT), the technique of least-squares deconvolution (LSD) was applied to the reduced spectra. LSD combines the information from many spectral lines to produce a single line profile, thereby providing an enormous multiplex gain in the SNR (e.g. Donati & Collier-Cameron 1997; Donati et al. 1997; Kochukhov, Makaganiuk & Piskunov 2010). A G2 line mask created from the Kurucz atomic data base and ATLAS9 atmospheric models (Kurucz 1993) was used to compute the average line profile for both stars. Tables 2 and 3 lists the SNR for each individual Stokes *V* LSD profile.

In order to correct for the minor instrumental shifts in wavelength space due to atmospheric temperature or pressure fluctuations, each spectrum was shifted to match the centroid of the Stokes *I* LSD pro-

Table 3. Journal of spectropolarimetric observations of HD 29615 using the AAT.

UT date	UT middle	Exp. time ¹ (s)	Mean SNR for Stokes V LSD profiles
2009 Nov 25	11:03:28	4 × 750	5567
2009 Nov 25	13:04:01	4 × 750	6337
2009 Nov 25	16:29:33	4 × 750	4908
2009 Nov 27	10:23:36	4 × 750	6171
2009 Nov 27	13:28:05	4 × 750	6978
2009 Nov 27	16:28:02	4 × 750	5610
2009 Nov 28	10:10:47	4 × 750	3821
2009 Nov 28	13:13:08	4 × 750	5971
2009 Nov 28	16:15:29	4 × 750	4280
2009 Nov 29	10:08:37	400 + 3 × 750	5785
2009 Nov 29	13:23:08	4 × 750	4604
2009 Nov 29	16:23:23	4 × 750	3493
2009 Nov 30	11:05:48	4 × 750	3283
2009 Nov 30	16:18:04	4 × 750	3713
2009 Dec 01	11:02:55	4 × 750	6353
2009 Dec 01	14:13:39	4 × 750	4961
2009 Dec 02	10:36:24	4 × 750	6158
2009 Dec 02	13:04:01	4 × 750	6176
2009 Dec 02	16:03:39	4 × 750	4651
2009 Dec 03	10:27:35	4 × 750	4228
2009 Dec 03	13:33:32	4 × 750	6312

Note. ¹Each sequence consists of four sub-exposures with each sub-exposure being 750 s (for example).

file of the telluric lines contained in the spectra, as was performed by Donati et al. (2003a) and Marsden et al. (2006). Further information on LSD can be found in Donati et al. (1997) and Kochukhov et al. (2010).

4 CHROMOSPHERIC ACTIVITY INDICATORS

Chromospheric activity can be determined using the Ca II H&K, Ca II infrared triplet (IRT) and H α spectral lines. The two Ca II H&K absorption lines are the most widely used optical indicators of chromospheric activity. There have been a number of long-term monitoring studies of the variation of Ca II H&K in solar-type stars spanning several decades. One study is the Mount Wilson Ca H&K project (e.g. Wilson 1978; Duncan et al. 1991). From this survey, differential rotation and solar-like activity cycles have been inferred on a number of solar-type stars (e.g. Baliunas et al. 1985; Donahue & Baliunas 1992; Donahue 1993; Donahue & Baliunas 1994).

The source functions of the Ca II H&K lines are collisionally controlled and hence are very sensitive to electron density and temperature. The Ca II IRT lines share the upper levels of the H&K transitions and are formed in the lower chromosphere (e.g. Montes et al. 2004). The H α spectral line is also collisionally filled in as a result of the higher temperatures and is formed in the middle of the chromosphere and is often associated with plages and prominences (e.g. Thatcher & Robinson 1993; Montes et al. 2004).

The Ca II H&K and Ca II IRT spectral lines were observed for HD 35296 but not for HD 29615 as the spectral range of SEMPOL does not extend far enough into the respective regions to permit monitoring of these diagnostic lines.

4.1 TBL activity indices for HD 35296

Morgenthaler et al. (2012) previously reported that the spectra in the region of the Ca II H&K are not well normalized by the pipeline reduction due to the dense distribution of photospheric lines. However, we did not adopt their method as a number of tests showed that simply removing the overlapping section of the order provided commensurate results as renormalizing the spectra.

The N_{CaIIHK} -index for HD 35296 was determined using the method as explained in Wright et al. (2004). The resulting N_{CaIIHK} -index was converted to match the Mount Wilson S -values (Duncan et al. 1991) using the transformation as follows:

$$S\text{-index} = \frac{C_1 H + C_2 K}{C_3 V_{\text{HK}} + C_4 R_{\text{HK}}} + C_5, \quad (1)$$

where H and K is the flux determined in the line cores from the two triangular bandpasses with a full-width at half-maximum (FWHM) of 0.1 nm. Two 2-nm-wide rectangular bandpasses R_{HK} and V_{HK} , centred on 400.107 and 390.107 nm, respectively, were used for the continuum flux in the red and blue sides of the H and K lines. The transformation coefficients were determined by Marsden et al. (2014) by matching 94 stars that were common to both the TBL data base and that of the Mount Wilson project. These coefficients were $C_1 = 12.873$, $C_2 = 2.502$, $C_3 = 8.877$, $C_4 = 4.271$ and $C_5 = 1.183 \times 10^{-3}$.

Two further activity indices were determined using the $\text{H}\alpha$ spectral line and the Ca II IRT lines. The continuum was checked against that of the continuum of the synthetic normalized spectrum from

the POLLUX data base (Palacios et al. 2010). In both cases, the continuum matched reasonably well and hence was not corrected. The TBL $\text{H}\alpha$ -index, based on Gizis, Reid & Hawley (2002), was determined using

$$N_{\text{H}\alpha}\text{-index} = \frac{F_{\text{H}\alpha}}{V_{\text{H}\alpha} + R_{\text{H}\alpha}}, \quad (2)$$

where $F_{\text{H}\alpha}$ is the flux determined in the line cores from the triangular bandpass with an FWHM of 0.2 nm. Two 0.22-nm-wide rectangular bandpasses $V_{\text{H}\alpha}$ and $R_{\text{H}\alpha}$, centred on 655.885 and 656.730 nm, respectively, were used for the continuum flux in the red and blue sides of the $\text{H}\alpha$ line. The TBL Ca IRT index, following Petit et al. (2013), was determined using

$$N_{\text{CaIRT}}\text{-index} = \frac{\sum F_{\text{IRT}}}{V_{\text{IRT}} + R_{\text{IRT}}}, \quad (3)$$

where $\sum F_{\text{IRT}}$ is the total flux measured in the line cores of the three spectral lines, 849.8023, 854.2091 and 866.2141 nm using triangular bandpasses with an FWHM of 0.1 nm. Two 0.5-nm-wide rectangular bandpasses V_{IRT} and R_{IRT} , centred on 847.58 and 870.49 nm, respectively, were used for the continuum flux in the red and blue sides of the Ca II IRT spectral lines.

Fig. 1 shows the variation in the Ca II H&K lines, Ca II IRT and $\text{H}\alpha$ spectral lines during 2007 (left-hand panels) and 2008 (right-hand panels) for HD 35296. The epoch for the 2007 data was set to the middle of the observation run whereas the epoch of the 2008 data was set to 104 stellar rotations later on and was chosen to be close to

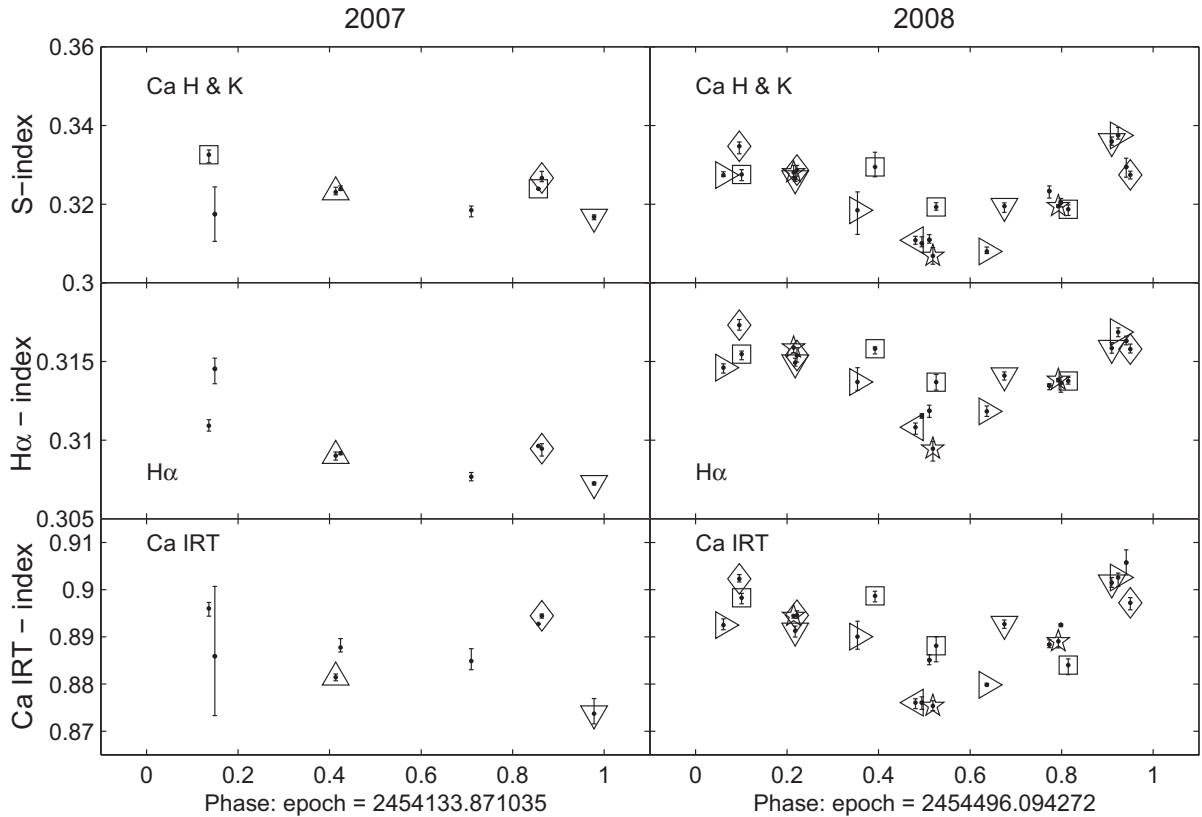


Figure 1. The variation in the Ca II H&K lines (upper), $\text{H}\alpha$ (middle) and Ca II IRT (lower) spectral lines during 2007 (left) and 2008 (right) for HD 35296. The index was measured for each spectrum, and then combined in sets of four, coinciding with a cycle of four sub-exposures as explained in Section 3.1. The average of these four indices was determined with the error bar being the minimum and maximum values for that set. The rotational period used was 3.48 d. The observing run covered ~ 4.3 rotations in 2007 and ~ 7.7 rotations in 2008. The symbols represent the respective rotations: ‘·’ only = first, ‘◊’ = second, ‘◻’ = third, ‘△’ = fourth, ‘▽’ = fifth, ‘◁’ = sixth, ‘▷’ = seventh and ‘☆’ = eighth rotation.

Table 4. HD 35296: average activity indices using the Ca II H&K, H α and Ca II IRT spectral lines. The error estimate is based on the range of values during each observing run.

Index	2007	2008
S -index ¹	0.323 ± 0.008	0.322 ± 0.016
$N_{H\alpha}$	0.310 ± 0.004	0.314 ± 0.004
N_{CaIRT}	0.887 ± 0.011	0.891 ± 0.015

Note. ¹The resulting N_{CaHK} -index was converted to match the Mount Wilson S -values (Duncan et al. 1991) using the transformation shown in equation (1).

the middle of the 2008 observation run, as explained in Section 5.2. The index was measured for each spectrum, and then combined in sets of four, coinciding with a cycle of four sub-exposures as explained in Section 3.1. The average of these four indices was determined with the error bar being the minimum and maximum values for that set. The data from 2007 showed limited variation, either due to the reduced coverage or a more homogeneous chromosphere. In contrast, in 2008, HD 35296 exhibited greater modulation of the S -index, Ca IRT index and H α -index while the average remained very similar with an S -index for 2007 of 0.323 ± 0.008 and for 2008 of 0.322 ± 0.016 . This is consistent, within error limits, with the average S -index of 0.308 ± 0.07 from the Mount Wilson survey (Duncan et al. 1991). Using the transformation values from Rutten (1984), $\log R'_{HK}$ was determined to be -4.45 ± 0.03 . This was an average value of the S -index over the observing runs with the error based on the minimum and maximum values. Table 4 shows the average S -index, $N_{H\alpha}$ and N_{CaIRT} indices for 2007 and 2008. Each value is the average over the observing run with the error showing the variation during this time, most likely as a result of modulation due to the rotation of the star.

4.2 AAT H α activity index for HD 29615

The H α spectral line was used as a chromospheric indicator for HD 29615. A similar approach, as explained in Section 4.1, was applied to the AAT data. The overlapping sections of the AAT spectra were removed and the continuum checked against a synthetic spectrum obtained from the POLLUX data base. In all cases, the continuum near the H α spectral line closely matched the synthetic spectra. Equation (2) was then used to determine the H α -index for HD 29615. Fig. 2 shows how this H α -index varied over the rotation period of HD 29615. The error bars indicate the range of the measurement during a cycle of four sub-exposures, as explained in Section 3.1. This supports the variable nature of the mid-level chromosphere, first observed by Waite et al. (2011a).

5 IMAGE RECONSTRUCTION

Surface images of these moderately rotating stars were generated through the inversion of a time series of LSD profiles of Stokes I (brightness images) or Stokes V (magnetic images). The ZDI code used was that of Brown et al. (1991) and Donati & Brown (1997). Because this inversion process is an ill-posed problem where an infinite number of solutions are possible when fitting to the noise level, this code implements the Skilling & Bryan (1984) maximum-entropy optimization that produces an image with the minimum amount of information required to fit the data to the noise level.

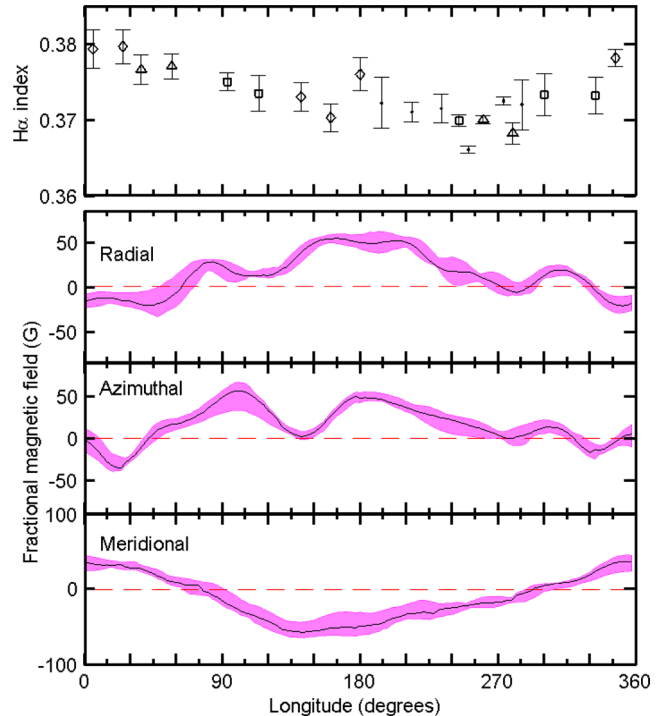


Figure 2. The top panel represents the variation in the H α -index as a function of longitude for HD 29615 (see Section 4.2). The observing run covered ~ 3.5 rotations. The symbols represent the respective rotations: ‘.’ = first, ‘◊’ = second, ‘□’ = third and ‘△’ = fourth rotation. The bottom three panels represent the variation in magnetic field strength for each configuration as a function of longitude (see Section 6.1). The shaded regions show the variation in the strength at each longitude as determined by varying $v \sin i$, inclination angle, Ω_{eq} and $\Delta\Omega$ within the limits of their respective accuracy. The epoch was set to MHJD = 55165.011060 with a rotational period of 2.34 d.

5.1 Brightness image of HD 29615

Brightness images were not reconstructed for HD 35296 as the $v \sin i$ of 15.9 km s^{-1} is below the usual limit for Doppler imaging (DI). In contrast, the observed intensity profiles for HD 29615 contained sufficient information for both mapping and a measurement of differential rotation using spot features.

A two-temperature model, one being the temperature of the quiet photosphere while the second is that of the cool spots, has been used to reconstruct the brightness image for HD 29615. Synthetic Gaussian profiles were used to represent the profiles of both the spot and photosphere. Unruh & Collier Cameron (1995) showed that the use of these synthetic profiles provides brightness maps that are very similar to those maps created by using profiles from slowly rotating stars of commensurate temperature. Hence, many authors now adopt this approach (e.g. Petit et al. 2004b; Marsden et al. 2005, 2006, 2011a,b; Waite et al. 2011b). Using the relationship between photospheric and spot temperature provided by Berdyugina (2005), the spot temperature of HD 29615 was estimated to be 3920 K.

The imaging code was used to establish the values of a number of basic parameters, including the star’s projected rotational velocity, $v \sin i$, and radial velocity, v_{rad} . This was achieved by systematically varying each parameter in order to minimize the reduced- χ^2 (χ_r^2) value (e.g. Marsden et al. 2005; Jeffers & Donati 2008). These key stellar parameters were determined with initially v_{rad} and then $v \sin i$. This sequence was repeated each time additional parameters, such

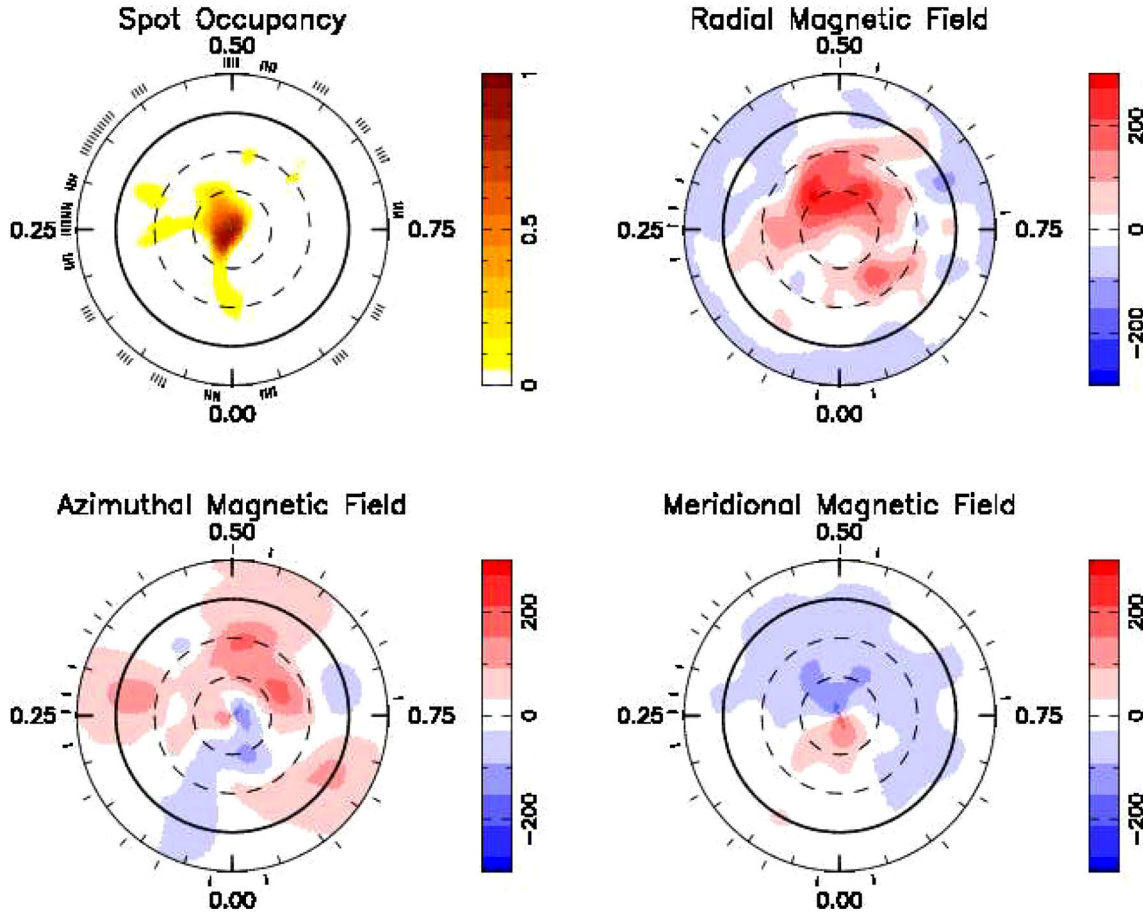


Figure 3. The maximum-entropy brightness and magnetic image reconstructions for HD 29615. These maps are polar projections extending down to -30° . The bold lines denote the equator and the dashed lines are $+30^\circ$ and $+60^\circ$ latitude parallels. The radial ticks indicate the phases at which this star was observed and the scale of the magnetic images is in gauss. Differential rotation, as measured using the Stokes I and V profiles, respectively, has been incorporated into the reconstruction of the maps. The spot map has a spot coverage of 2.6 per cent while the global magnetic field strength is 81.6 G. The epoch was set to MHJD = 55165.011060 with a rotational period of 2.34 d.

as inclination or differential rotation parameters, were modified as a result of the imaging process.

The inclination angle for HD 29615 was estimated using the bolometric corrections of Bessell, Castelli & Plez (1998) and was confirmed using the imaging code. This value was determined to be $65_{-10}^{+5}^\circ$. The minimum angle of $\sim 50^\circ$ assumed a stellar radius of $1.2 R_\odot$ (Messina et al. 2010). A linear limb-darkening coefficient of 0.62 was used (Sing 2010). The full set of parameters that gave the minimum χ_r^2 value of 0.45 are shown in Table 1 and were adopted when producing the final DI map as shown in the top-left panel of Fig. 3. A χ_r^2 value less than 1 is possible as the SNR calculated for the LSD Stokes I profiles are underestimated (e.g. Petit et al. 2004b; Marsden et al. 2011a). Nevertheless, this has no impact on the final brightness maps. The maximum-entropy fits to the Stokes I LSD profiles for HD 29615 with the measured surface differential rotation incorporated into the analysis are shown in Fig. 4. Deviations of the model profile from the observed profile are shown in the dynamic spectrum displayed in Fig. 5. To produce this dynamic spectrum, each observed LSD profile was normalized, and then subtracted from the associated normalized model profile with the residual profile being plotted as the dynamic spectrum. The scale of this dynamic spectrum is $\pm 4 \times 10^{-3}$ or ≈ 0.4 per cent of the intensity of the line profile. The small residuals indicate that

the majority of the large-scale features can be accurately modelled. However, there is a consistent mismatch between the modelled and original data as evidenced by a brighter band near the red wing of the dynamic spectrum. This indicates that the modelled data have not incorporated information from the wings of the original line profiles. This is advantageous in that modelling of that part of the line profile may have led to spurious banding in the resulting image (Unruh & Collier Cameron 1995).

5.2 Magnetic images

The magnetic topology was determined for both HD 35296 and HD 29615 using ZDI. ZDI requires high-SNR data as the polarization signature is typically less than 0.1 per cent of the total light intensity (Donati et al. 1997). The Stokes V data were used to reconstruct radial, azimuthal and meridional fields coinciding with the three vector fields in spherical geometry. The modelling strategy of Donati & Brown (1997) was used to construct the magnetic field topology on both stars. ZDI only measures the large-scale magnetic field as the small-scale magnetic fields cannot be recovered as the positive and negative magnetic fields within the resolution element are likely to cancel each other out. The mapping procedure involved uses the spherical harmonic expansions of the surface magnetic field,

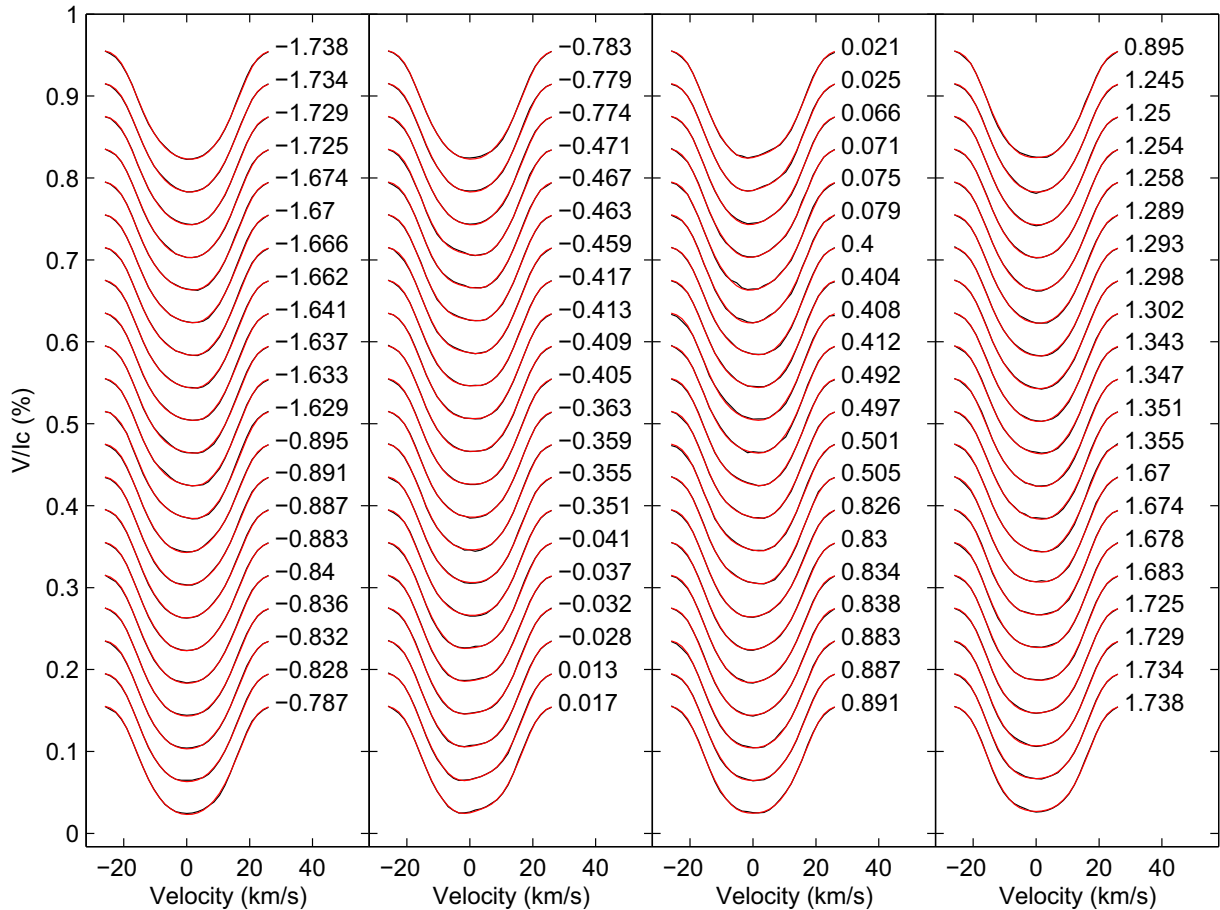


Figure 4. The maximum-entropy fits to the Stokes I LSD profiles for HD 29615 with the measured surface differential rotation incorporated into the analysis. The red lines represent the modelled lines produced by the DI process whereas the black lines represent the actual observed LSD profiles. Each successive profile has been shifted down by 0.020 for graphical purposes. The rotational cycle at which the observation took place is indicated to the right of each profile. The epoch was set to MHJD = 55165.011060 with a rotational period of 2.34 d.

as implemented by Donati et al. (2006). The maximum spherical harmonic expansion $\ell_{\max} = 11$ was selected for HD 35296 while $\ell_{\max} = 14$ was used for HD 29615. These were the minimum values where any further increase did not produce any difference in the magnitude and topology of the magnetic field recovered.

The magnetic maps for HD 29615 are shown in Fig. 3 while the associated fits between the modelled data and the actual LSD profiles are shown in Fig. 6. The χ_r^2 value of the magnetic models for HD 29615 was 1.25, showing that the fit accuracy was very close to reaching the noise level of the data.

The magnetic maps for HD 35296 for the 2007 and 2008 data sets are shown in Fig. 7 with the associated fits between the modelled data and the actual profiles shown in Fig. 8. The LSD profile taken on 2007 February 02 of HD 35296 was excluded from the mapping process due to the relatively poor SNR. Including these data made no difference to the resulting magnetic maps and field configuration but did make a marginal degradation of the total magnetic field strength (by 0.1 G). In each case, the minimum χ_r^2 value of the magnetic models was set to 1.0.

The full set of parameters used to produce these maps, including differential rotation (see Section 5.3), are listed in Table 1. Due to the length of time between the observing runs for HD 35296, the phases for the 2007 run were calculated using an epoch of the Modified Heliocentric Julian Date (where MHJD = HJD - 2400000.0) of

54133.871035 whereas the 2008 run used an epoch of MHJD = 54496.094272. This 2008 epoch was selected as it was close to the mid-point of the observing run, but was an integer number of rotations since the mid-point of the 2007 run based on the 3.48 d period.

5.3 Differential rotation

There have been a number of different methods by which differential rotation has been measured on stars. Reiners & Schmitt (2003a,b) have used a Fourier transform method to derive the parameters for rapidly rotating inactive F-type/early G-type stars. They produce a deconvolved line profile from the stellar spectrum and determine the ratio of the second and first zero of the resulting Fourier transform. This ratio is a measure of the magnitude of the differential rotation on the stellar surface. However, for active young stars with significant asymmetry within the line profiles, this technique is not as effective. Differential rotation of active, rapidly rotating stars can be estimated by tracking spot features at different latitudes on the surface of the star from multiple Doppler images (Collier Cameron, Donati & Semel 2002). Alternatively, cross-correlation techniques can be used on two independent Doppler images (Donati & Collier-Cameron 1997). Finally, a solar-like differential rotation law, as defined in equation (4), can be applied to measure the

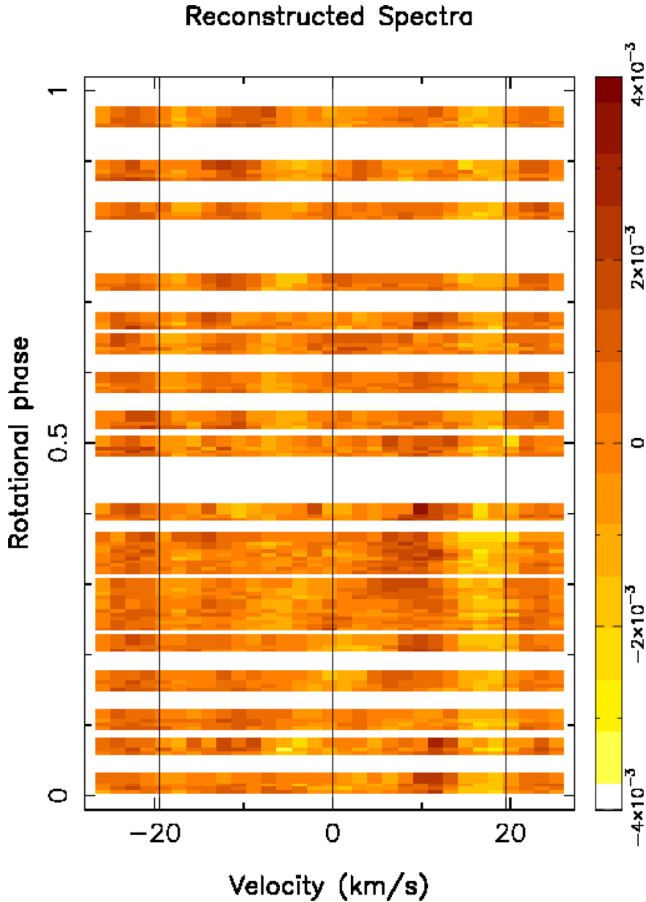


Figure 5. Dynamic spectrum of the residual plot for the Stokes I LSD profiles for HD 29615. Each LSD profile was normalized and subtracted from the associated normalized model profile.

rotation of a number of solar-type stars (e.g. Petit, Donati & Collier Cameron 2002; Donati, Collier Cameron & Petit 2003b; Petit et al. 2004b; Barnes et al. 2005; Marsden et al. 2005, 2006),

$$\Omega(\theta) = \Omega_{\text{eq}} - \Delta\Omega \sin^2\theta, \quad (4)$$

where $\Omega(\theta)$ is the rotation rate at latitude θ in rad d^{-1} , Ω_{eq} is the equatorial rotation rate, and $\Delta\Omega$ is the rotational shear between the equator and the pole. This technique uses fixed information content of the spot coverage (Stokes I) or magnetic field strength (Stokes V) for the maps while systematically adjusting the differential rotation parameters, Ω_{eq} and $\Delta\Omega$. The best fit to the data, using χ^2 minimization techniques, is subsequently determined by fitting a paraboloid to the reduced- χ^2 landscape thereby measuring the differential rotation parameters. It is this χ^2 minimization technique that has been adopted for this work as it is best suited to the longer time-base data sets presented in this paper.

Using the magnetic signatures, HD 35296 has an equatorial rotational velocity, Ω_{eq} , of $1.804 \pm 0.005 \text{ rad d}^{-1}$ with a rotational shear, $\Delta\Omega$, of $0.22^{+0.04}_{-0.02} \text{ rad d}^{-1}$. Using the brightness features, HD 29615 has an equatorial rotational velocity, Ω_{eq} , of $2.68^{+0.06}_{-0.02} \text{ rad d}^{-1}$ with a rotational shear, $\Delta\Omega$, of $0.07^{+0.10}_{-0.03} \text{ rad d}^{-1}$. Using the magnetic features, HD 29615 has an equatorial rotational velocity, Ω_{eq} , of $2.74^{+0.02}_{-0.04} \text{ rad d}^{-1}$ with a rotational shear, $\Delta\Omega$, of $0.48^{+0.11}_{-0.12} \text{ rad d}^{-1}$ (see Table 1).

The errors for the differential rotation measurements were calculated by individually varying stellar parameters such as spot

occupancy (for Stokes I : ± 10 per cent) or global magnetic field (for Stokes V : ± 10 per cent), inclination angle ($\pm 5^\circ$ for HD 35296 and $+5^\circ$ and -10° for HD 29615) and $v \sin i$ ($\pm 0.1 \text{ km s}^{-1}$) and determining the minimum $\Omega_{\text{eq}} - \Delta\Omega$ pair from each of the reduced- χ^2 landscapes generated. Figs 9 and 10 show the reduced- χ^2 landscapes for the optimum set of parameters, as listed in Table 1. Superimposed on these are the individual $\Omega_{\text{eq}} - \Delta\Omega$ pairs derived from this variation of stellar parameters, with the error bars being 1σ errors in the paraboloid fit. The final ellipse was generated to encompass all the differential rotation values. The true error bars may be slightly larger than this due to intrinsic spot evolution during the data collection (e.g. Morgenthaler et al. 2012). The differential rotation parameters determined for HD 35296 for the 2008 observing run were used in the mapping process for the 2007 data as no differential rotation was able to be determined for this data set due to the limited number of exposures.

6 DISCUSSION

HD 35296 and HD 29615 are two moderately rapidly rotating young Sun-like stars that display rotational variation in their chromospheric activity. In this paper, we have determined the surface topology of both stars revealing complex magnetic fields and high levels of surface differential rotation.

6.1 Chromospheric activity

Chromospheric activity was determined using the Ca II H&K, Ca II IRT and H α spectral lines for HD 35296 while only the H α line was used for HD 29615 as the spectral range of SEMPOL did not extend far enough into the respective regions to permit monitoring of the Ca II diagnostic lines. Table 4 shows the average activity indices in 2007 and 2008 for HD 35296. The average S -index was 0.322 ± 0.016 while the average H α -index, $N_{\text{H}\alpha}$, 0.312 ± 0.006 and the average Ca II IRT index, N_{CaIRT} , was $0.889^{+0.017}_{-0.013}$. Fig. 1 demonstrates the variable nature of the activity of HD 35296. In 2007, the chromosphere was more homogeneous with respect to phase. The large error bar at phase ~ 0.15 is the result of a poor SNR observation. The amplitude of the modulation in the Ca II H&K and H α indices is less than that observed in 2008. This would indicate that HD 35296 is more active during the 2008 epoch. In addition, the error bars on each of the data points do not overlap indicating that the chromosphere not only varied as a function of rotation, but also from one rotation to the next. This is clearly observed in all three chromospheric diagnostic lines. The conclusion is that the chromosphere of HD 35296 is highly variable over a one-month interval of approximately eight stellar rotations.

S -index measurements are also available from Baliunas et al. (1995), where data were obtained between 1966 and 1991. The average S -index from the Baliunas sample is 0.33 ± 0.02 and the $\log R'_{\text{HK}}$ is -4.36 ± 0.04 . Mount Wilson data were not available from 1991 onwards but fortunately Lowell observatory started a long-term Ca II H&K monitoring programme where HD 35296 was observed from 1994 to 2008 (Hall et al. 2009). All available S -index values scaled to the Mount Wilson system are shown in Fig. 11. HD 35296 exhibits a gradual decrease in its S -index from 1966 to 1980 and shows a relatively flat trend from 1980 onwards. Interestingly, during the low-activity period the S -index does exhibit small variations. The long-term variations also indicate a probable long cyclic period which was also determined by Baliunas et al. (1995). No error estimates are available for the Lowell catalogue.

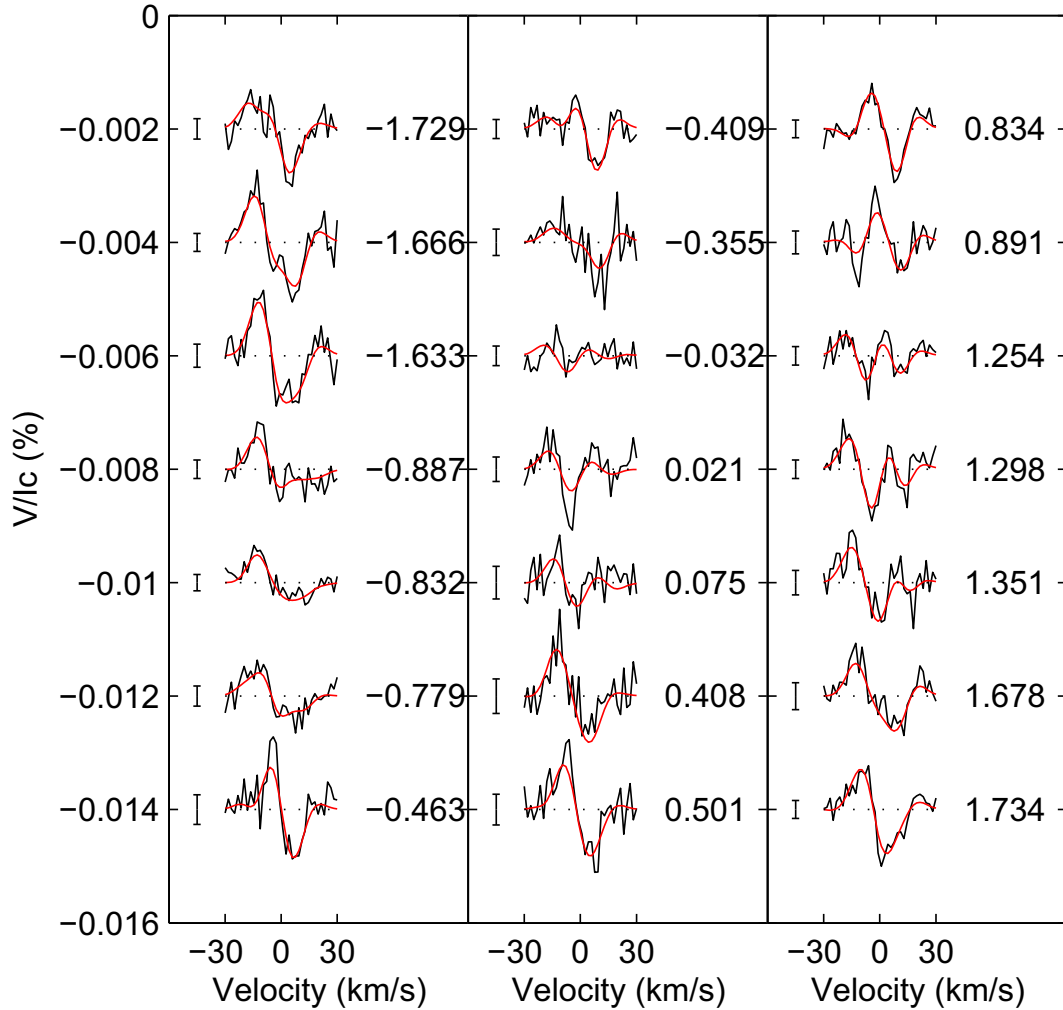


Figure 6. The maximum-entropy fits to the Stokes V LSD profiles for HD 29615 with the measured surface differential rotation incorporated into the analysis. The black lines represent the observed Zeeman signatures, while the red lines represent the modelled lines. Each successive profile has been shifted down by 0.002 for graphical purposes. The minimum χ_r^2 value was set to 1.25. The rotational phases at which the observations took place are indicated to the right of each profile. The error bars to the left of each profile are $\pm 0.5\sigma$. The epoch was set to MHJD = 55165.011060 with a rotational period of 2.34 d.

The average $H\alpha$ -index for HD 29615 is 0.373 ± 0.008 . As indicated in Section 4, the $H\alpha$ spectral line is often associated with plages and prominences (e.g. Thatcher & Robinson 1993; Montes et al. 2004). There was evidence of the existence of plage-like behaviour on HD 29615 when considering the $H\alpha$ emission as shown in Fig. 2 (top panel). If longitude increases with phase with 0° longitude corresponding to 0.0 phase, then this $H\alpha$ emission reaches a maximum at longitude $\sim 220^\circ$. There appears to be enhanced magnetic features in the radial magnetic field trailing slightly, at approximately 180° , as shown in Fig. 2. The three lower panels in Fig. 2 show the fractional magnetic field strength as a function of longitude around the star for the radial, azimuthal and meridional magnetic field components. These were calculated using

$$F(\varphi) = B(\varphi)d\varphi, \quad (5)$$

where $F(\varphi)$ is the fractional magnetic field strength at longitude φ , $B(\varphi)$ is the average magnetic field strength at longitude φ and $d\varphi$ is the width of each latitude ring. These enhanced features can also be seen in the resulting map in Fig. 3 (top-right panel). We can speculate that the enhanced positive radial magnetic field is

contributing to the activity in the mid-level chromosphere, perhaps with the production of plages or even prominences at mid-latitude, very similar in location to those features observed on the Sun.

6.2 Brightness and magnetic maps

The results presented in this paper show that HD 35296 and HD 29615 are young, Sun-like stars whose moderately rapid rotation has led to very complex large-scale surface magnetic field topology. As discussed in Section 5, brightness images were not produced for HD 35296 due to its relatively low $v \sin i$ with the LSD intensity profiles not being sufficiently deformed by any surface features present to recover reliable spot information using DI. The brightness map for HD 29615, in Fig. 3 (top-left panel), shows a dominant polar spot. This polar spot is slightly off-centred with features extending to $\sim 60^\circ$ latitude for phases between, ϕ , 0.0 and 0.5, but not evident for $\phi = 0.5-1.0$. While the polar spot is very prominent, there appears limited spot coverage at mid- to lower latitudes with a small number of features observed at $\phi \sim 0, 0.25-0.3$ and $0.55-0.65$. The features at $\phi \sim 0$ and ~ 0.25 may not be reliable as the dynamic spectrum

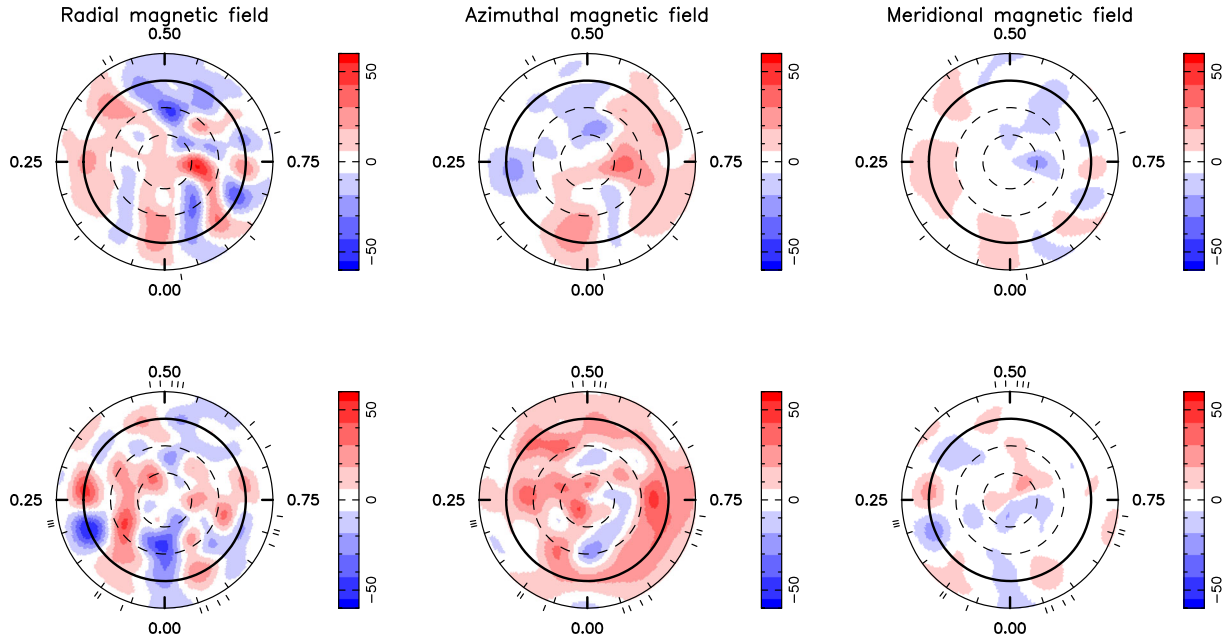


Figure 7. Magnetic imaging of the large-scale field for HD 35296 from both the 2007 (top series) and 2008 (bottom series) observing runs. These maps are polar projections, as explained in Fig. 3. The 2007 global magnetic field was 13.4 G whereas the 2008 field was 17.9 G. The epoch was set to MHJD = 54133.871035 for the 2007 data and MHJD = 54496.094272 for the 2008 data, with a rotational period of 3.48 d.

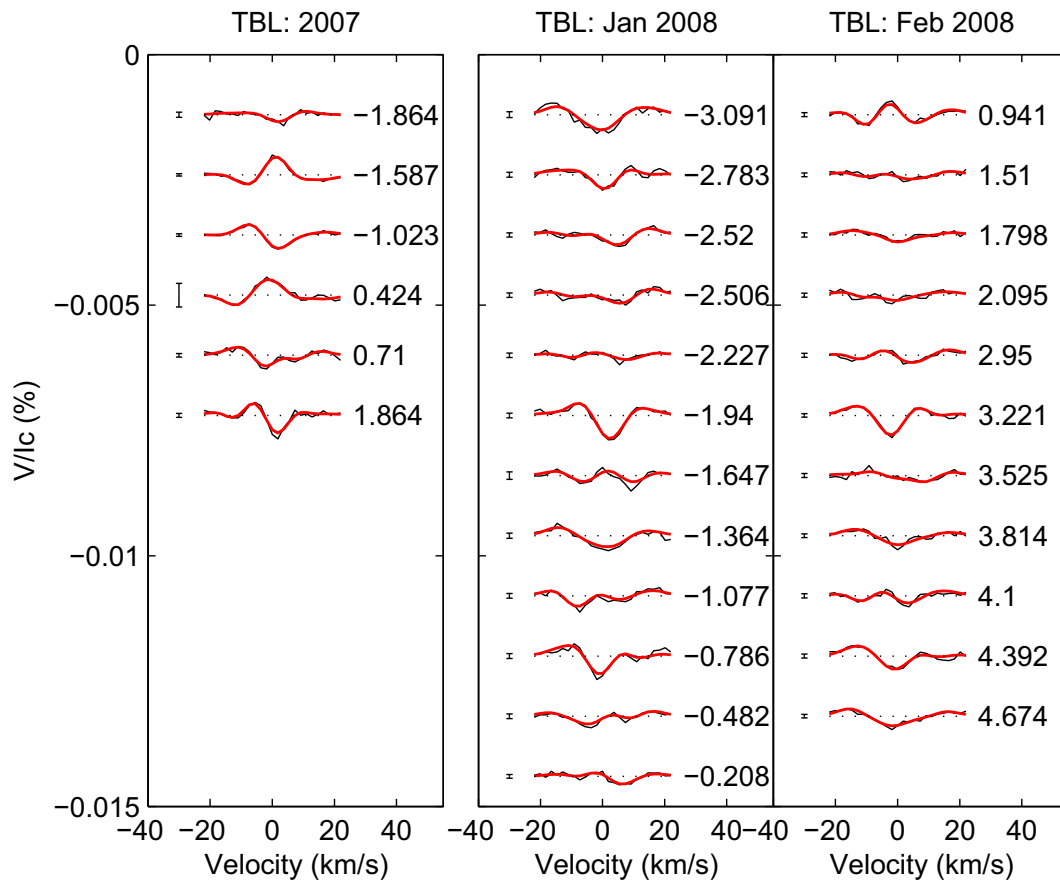


Figure 8. The maximum-entropy fits to the LSD profiles for HD 35296 during 2007 (left-hand panel) and 2008 (right-hand panel), with differential rotation incorporated into the analysis. The observed Zeeman signatures are shown in black while the fit to the data is shown as red lines. The rotational cycle and $\pm 0.5\sigma$ error bars of each observation are shown next to each profile. Each profile has been shifted down by 0.0012 for clarity. The minimum χ_r^2 value used was 1.0. The LSD profile obtained on 2007 February 02 was excluded from the mapping process due to its relatively low SNR. The rotational period used was 3.48 d.

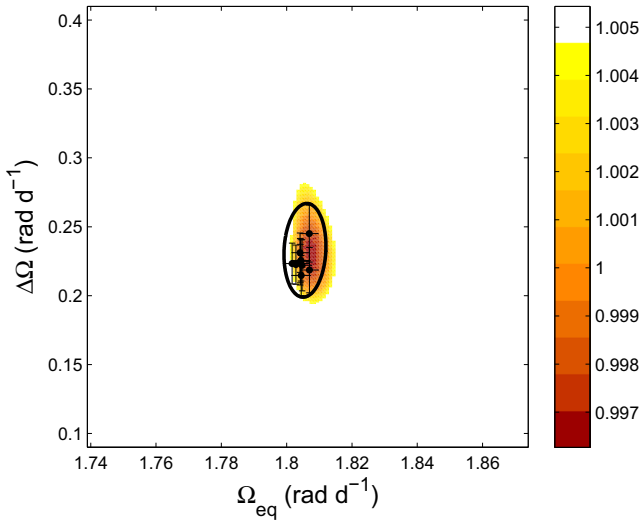


Figure 9. Differential rotation using Stokes V : HD 35296 in 2008. The contour plot is a 1σ projection using the optimum set of parameters, as listed in Table 1. The darker regions correspond to lower reduced- χ^2 values. Superimposed on this grid is the error ellipse (thick line) that encompasses a range of $\Omega_{\text{eq}}-\Delta\Omega$ pairs determined by varying such parameters as $v \sin i$, magnetic field strength and inclination. Each data point is the result of paraboloid fit of the reduced- χ^2 landscape for each individual differential rotation value. The error bars on each data point are 1σ errors in the paraboloid fit.

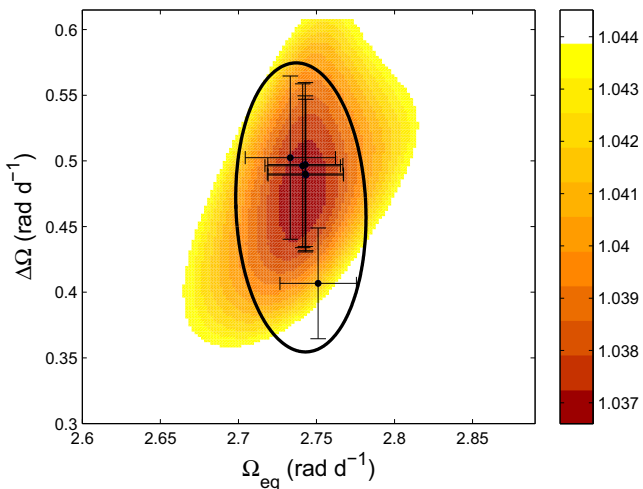


Figure 10. Differential rotation using Stokes V : HD 29615. The contour plot is a 1σ projection using the optimum set of parameters, as listed in Table 1. Superimposed on this grid is the error ellipse (thick line) encompassing the respective $\Omega_{\text{eq}}-\Delta\Omega$ pairs, as explained in Fig. 9. The error bars on each data point are 1σ errors in the paraboloid fit.

shown in Fig. 5 displays a dark diagonal band moving from the blue wing to the red wing. This indicates that the modelled data may have incorporated spots at this phase that were not present in the original data and hence could not accurately constrain the latitude of these two features. Unruh & Collier Cameron (1997) note that spectroscopy extracts the higher latitude features but cannot discriminate lower latitude features at latitudes $\lesssim 30^\circ$. However, the paucity of spots at mid- to lower latitudes is dissimilar to other more rapidly rotating solar-type stars like He 699 (V532 Per, SpType: G2-3V; Jeffers, Barnes & Collier Cameron 2002), HD 106506 (SpType:

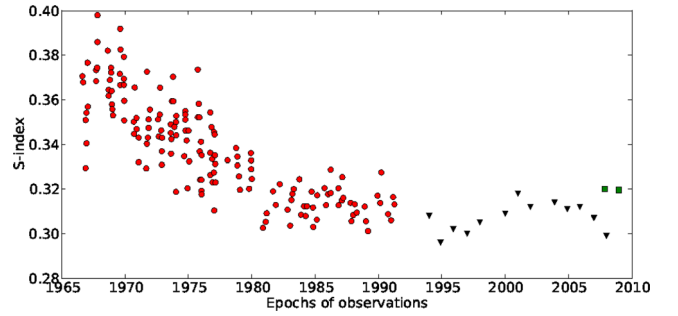


Figure 11. The long-term Ca II H&K S -index data for HD 35296. The Mount Wilson data taken from 1966 to 1991, shown as \circ (Baliunas et al. 1995) while the Lowell data taken from 1994 to 2008, shown as \blacktriangledown (Hall et al. 2009). Additionally, the two values shown as \square were determined by this work.

G1V; Waite et al. 2011b) and HD 141943 (SpType: G2; Marsden et al. 2011a) that appear to have spots covering all latitudes and phases.

The magnetic maps for HD 29615, in Fig. 3, show azimuthal, meridional and radial magnetic field structures. The azimuthal magnetic field is strongly positive although not a complete ring of field, unlike that observed on other solar-type stars such as HD 106506 (Waite et al. 2011b) and HD 141943 (Marsden et al. 2011a). The radial field is also strongly positive at higher latitudes, from approximately $+30^\circ$ to the pole. The maps for HD 35296 from 2007 and 2008 are shown in Fig. 7. Like HD 29615, HD 35296 displays a predominantly positive azimuthal magnetic field in both 2007 and 2008 while the radial and meridional fields show mixed polarity across the surface.

When using Stokes V without Stokes I , Q , U , there is crosstalk between the three magnetic field configurations, although the azimuthal field is the most robust with limited crosstalk. At high latitudes, ZDI can recover all three field components but at lower latitudes, in particular for stars with inclination angles greater than 50° , the crosstalk is from the meridional to radial field component (Donati & Brown 1997). This crosstalk appears stronger for HD 35296 when compared with HD 29615. This could be due to either a weaker magnetic field or fewer phases for each rotation for HD 35296 thereby affecting the code's ability to distinguish between the radial and meridional field components, particularly at lower latitudes. Rosén & Kochukhov (2012) have observed when using all four Stokes $IQUV$ parameters, the crosstalk between the components is significantly reduced. However, the linear polarization states (Stokes Q and U parameters) are significantly weaker than the Stokes V and are extremely difficult to observe on active cool stars such as HD 29615 and HD 35296 (e.g. Wade et al. 2000; Kochukhov et al. 2004).

6.3 Latitude dependence of the magnetic fields

The fractional magnetic field strength as a function of latitude for each orientation for HD 35296 and HD 29615 was determined using

$$F(\theta) = \frac{B(\theta)\cos(\theta)d\theta}{2}, \quad (6)$$

where $F(\theta)$ is the fractional magnetic field strength at latitude θ , $B(\theta)$ is the average magnetic field strength at latitude θ and $d\theta$ is the width of each latitude ring. The results are shown in Fig. 12. In

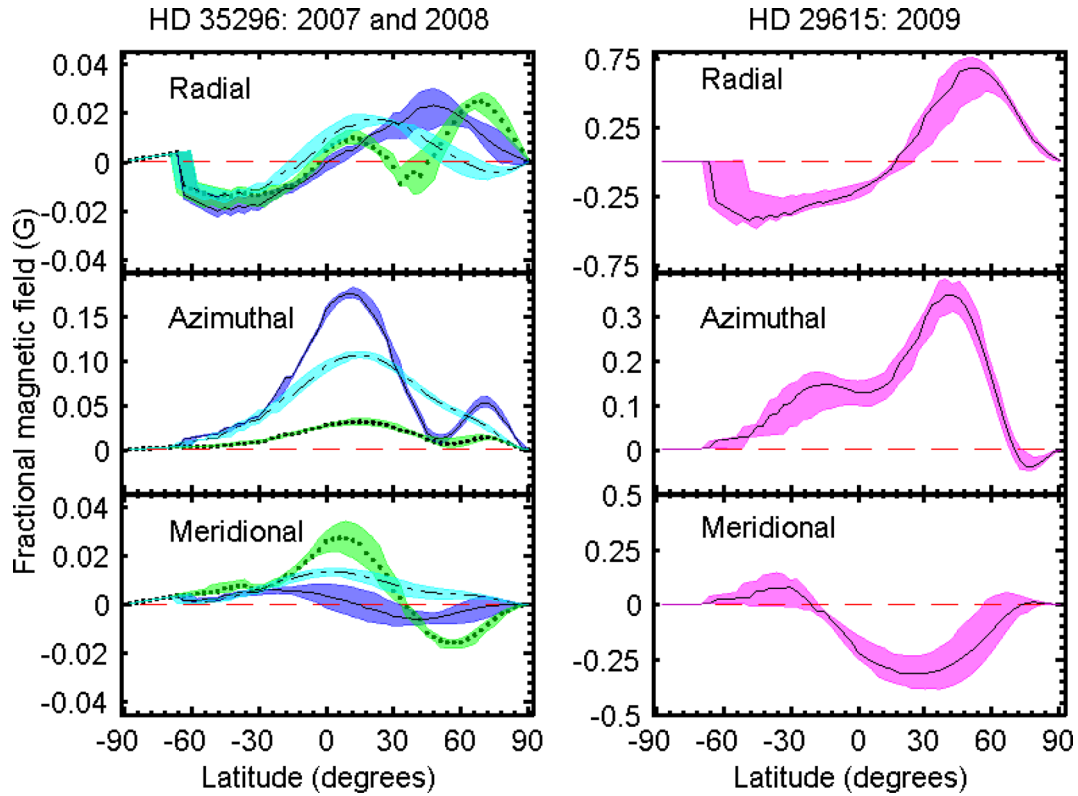


Figure 12. Variation of the respective magnetic field orientations for HD 35296 (left series of panels) and HD 29615 (right series of panels). The shaded regions show the variation in the strength at each latitude point as determined by varying $v \sin i$, inclination angle, Ω_{eq} and $\Delta\Omega$ within the limits of their respective accuracy (see Section 5.3). Considering HD 35296, the solid line with the dark blue shading is for 2008 data while the dotted line with the green shading is for the 2007 data. The dot-dashed line with cyan shading represents the 2008 data with reduced number of profiles approximately matching the number of profiles and phase of the 2007 data. The period used for HD 35296 was 3.48 d while the period used for HD 29615 was 2.34 d.

order to determine the robustness of each measurement, the $v \sin i$, v_{rad} , inclination angle, Ω_{eq} and $\Delta\Omega$ were varied, placing limits on the fractional magnetic field at each latitude for each of the orientations. These measured variations are shown by the shaded regions while the values for the optimum parameter set are shown as a solid line for the 2007 data and a dotted line for the 2008 data. HD 35296 displayed both positive and negative radial fields in 2007 but predominantly a positive field in 2008 whereas the azimuthal field remains a positive field for both epochs. Conversely, the radial field, at mid-latitudes, appears to have undergone a reversal of polarity from 2007 to 2008. This may be real or an artefact due to fewer profiles being used in the reconstruction.

To test this, we reduced the number of profiles in the 2008 data set, to match the same number of profiles and phase as that obtained in 2007. This had an impact on the strength of the global magnetic field (17.9 G reduces to 11.9 G) and the latitudinal distribution of the respective fields. The azimuthal field remained strongly positive, as shown in Fig. 12 (dot-dashed line with cyan colour). However, the radial field no longer shows a strong positive peak at $\sim 70^\circ$ latitude when compared with using the full number of profiles, although it does remain positive at these mid-latitudes. As a further test, maps were produced from the first two rotations, middle four rotations and final two rotations. This demonstrated the robust nature of the azimuthal magnetic field, although fewer profiles meant that the imaging code could not adequately recover the latitude of each feature. Nevertheless, the mid-latitude reversal in the radial field from 2007 to 2008 may well be real. The evidence is tantalizing but more data would be required before any definitive conclusion can

be drawn regarding any changes in the mid-latitude field polarity of HD 35296.

Comparing HD 35296 with HD 29615, it appears that the dominant azimuthal fields are restricted to the equatorial regions for HD 35296 whereas the similar fields dominate at higher latitudes for HD 29615. Both HD 35296 and HD 29615 have similar latitudinal distributions in the meridional and radial fields. Thus, both of these young, Sun-like stars with similar masses and $v \sin i$ have similar magnetic field configurations.

6.4 Magnetic field configurations

Large-scale magnetic fields on the Sun are considered to arise from the interplay between the poloidal and toroidal components in what is commonly referred to as the α - Ω dynamo (Babcock 1961). In the Sun, the toroidal component is understood to be confined to the interface between the radiative core and the convection zone (e.g. Charbonneau & MacGregor 1997; MacGregor & Charbonneau 1997). However, in solar-type stars, the toroidal component may manifest itself in the form of strong azimuthal magnetic fields on, or near, the surface of the star (e.g. Donati et al. 2003a; Petit et al. 2004b). Additionally, Petit et al. (2008) infer that a rotation period lower than ~ 12 d is necessary for the toroidal magnetic energy to dominate over the poloidal component. Both of these moderately rapidly rotating stars appear to have a large azimuthal component. These results are consistent with observations of more rapidly rotating stars exhibiting similarly strong azimuthal magnetic fields such as AB Doradus (SpType: K0V), LQ Hydrae (SpType: K0V)

and HR 1099 (SpType: K2:Vnk; Donati et al. 2003a), HD 171488 (SpType: G2V; Marsden et al. 2006; Jeffers & Donati 2008; Jeffers et al. 2011), HD 141943 (SpType: G2; Marsden et al. 2011b) and HD 106506 (SpType: G1V; Waite et al. 2011b). Observations of these strong surface azimuthal magnetic fields on active stars have been interpreted by Donati et al. (2003a) as a result of the underlying dynamo processes being capable of generating fields directly in the subsurface region (e.g. Dikpati et al. 2002) and could be distributed throughout the whole convection zone (e.g. Lanza, Rodonò & Rosner 1998).

The magnetic field on HD 35296 was predominantly poloidal in 2007, with $\sim 82^{+2}_{-1}$ per cent of the total magnetic energy. By 2008, the field had reorganized itself to an $\sim 50:50$ per cent poloidal–toroidal configuration. This is shown in Table 5 and in Fig. 7. Again there are two plausible reasons for this. One is that the magnetic topologies had significantly changed. Alternatively, simply using fewer profiles may be responsible for the observed changes. Reducing the number of profiles, as explained in Section 6.3, had only a minor effect on the balance of the poloidal–toroidal field configuration in 2008. This is shown in Table 5, where the full data set produced a poloidal–toroidal ratio of 50:50 per cent while the reduced data set produced a ratio of 48 to 52 per cent. Higher cadence data would be required to support the conclusion that the global magnetic field topology had significantly evolved during the course of one year on HD 35296. The second star, HD 29615, was observed to be strongly poloidal with 75^{+6}_{-5} per cent of the magnetic energy being held in this configuration. Of this, 58 per cent of the poloidal component is dipolar ($\ell = 1$). This is similar to other stars such as HD 76151 (SpType: G3V; Petit et al. 2008), τ Bootis (SpType: F6IV; Farés et al. 2009) and ξ Bootis (SpType: G8V; Morgenthaler et al. 2012) which are also strongly poloidal with complex fields with predominantly dipolar fields. Table 5 gives a full listing of the various components for both HD 35296 and HD 29615.

6.5 Differential rotation

Differential rotation was measured for HD 35296 and HD 29615. The differential rotation of HD 35296, using Stokes V, was measured for the 2008 data using the χ^2 minimization technique, as described in Section 5.3. Using the magnetic signatures, HD 35296 has an equatorial rotational velocity, Ω_{eq} , of $1.804 \pm 0.005 \text{ rad d}^{-1}$ with rotational shear, $\Delta\Omega$, of $0.22^{+0.04}_{-0.02} \text{ rad d}^{-1}$. Differential rotation was not observed on the 2007 data due to the limited number of profiles obtained. This $\Delta\Omega$ value is consistent with similar observations of other F-type stars by Reiners (2006) and Ammler-von Eiff & Reiners (2012); however, Reiners (2006) found no evidence of differential rotation using the Fourier transform method of line profile analysis on HD 35296. Another star that exhibits this discrepancy is the pre-main-sequence binary star HD 155555 (SpType = G5IV+K0IV) when Dunstone et al. (2008) measured differential rotation on both components while Ammler-von Eiff & Reiners (2012) could not detect differential rotation. Reiners (2006) conducted a direct comparison between the Fourier transform method and DI using HD 307938 (R58) in IC 2602. Marsden et al. (2005) used DI to measure a shear of $\Delta\Omega = 0.025 \pm 0.015 \text{ rad d}^{-1}$. Using the Fourier transform method, the threshold for solid-body rotation, q_2/q_1 , is 1.76, where q_1 and q_2 are the first two zeros of the line profile’s Fourier transform. Reiners (2006) argued that for a star with a large polar spot and small shear (such as R58), the spot has more influence on q_2/q_1 than small deviations from solid-body rotation. This does not answer the question why HD 35296’s differential rotation was measured using ZDI but not Fourier transform

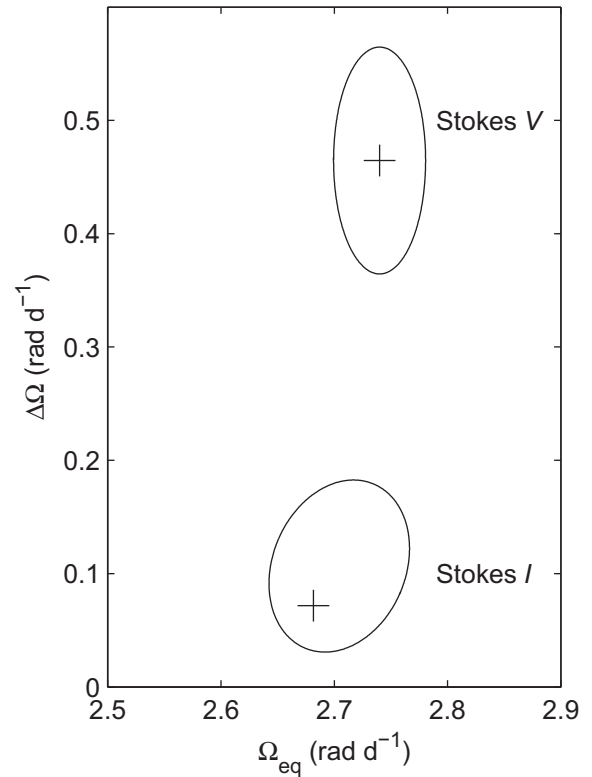


Figure 13. Differential rotation using Stokes *I* and *V* for HD 29615, including the associated variation ellipses (as explained in Section 5.3). The brightness (spot) features produce an equatorial rotational velocity, Ω_{eq} , of $2.68^{+0.06}_{-0.02} \text{ rad d}^{-1}$ with rotational shear, $\Delta\Omega$, of $0.07^{+0.10}_{-0.03} \text{ rad d}^{-1}$. Using the magnetic features observed, HD 29615 has an equatorial rotational velocity, Ω_{eq} , of $2.74^{+0.02}_{-0.04} \text{ rad d}^{-1}$ with rotational shear, $\Delta\Omega$, of $0.48^{+0.11}_{-0.12} \text{ rad d}^{-1}$.

method. Reiners (2006) measured $q_2/q_1 = 1.75$ (for HD 35296), only marginally less than solid-body rotation, yet this work measured a rotational shear, $\Delta\Omega$, of $0.22^{+0.04}_{-0.02} \text{ rad d}^{-1}$. One would expect this to give a $q_2/q_1 \sim 1.50$ to 1.60. This disparity in measured differential rotation could be real, or just reflects the fact that this work is based on Stokes *V* whereas the value of Reiners (2006) was derived from Stokes *I* data which often give lower values, as shown by the results for HD 29615. Alternatively, the Stokes *I*/LSD profiles of HD 35296 were not sufficiently deformed by spots to produce a detailed map whereas their presence may have affected the measurement in the Fourier domain.

The differential rotation measurement for HD 29615, using the magnetic features, indicates an equatorial rotational rate $\Omega_{\text{eq}} = 2.74^{+0.02}_{-0.04} \text{ rad d}^{-1}$ and shear $\Delta\Omega = 0.48^{+0.11}_{-0.12} \text{ rad d}^{-1}$. This rotational shear is relatively large although Reinhold, Reiners & Basri (2013) have measured larger rotational shear on active *Kepler* stars with temperatures commensurate with HD 29615 (see fig. 15 of that work). In contrast, the spot features provide a different value, namely $\Omega_{\text{eq}} = 2.68^{+0.06}_{-0.02} \text{ rad d}^{-1}$ and $\Delta\Omega$ of $0.07^{+0.10}_{-0.03} \text{ rad d}^{-1}$ (see Fig. 13). Donati et al. (2003b) noted that in some early K-dwarf stars, the level of differential rotation measured from brightness features is usually lower when compared with the levels measured when using magnetic features. Their interpretation of this variation is that the brightness features and the magnetic features are anchored at different depths within the convection zone of the star. This could also be the case here, though the difference in $\Delta\Omega$ that we measure for HD 29615 is more extreme than previously observed for other

Table 5. Magnetic quantities derived from the set of magnetic maps for HD 35296 and HD 29615. Both the poloidal and toroidal components are listed along with the relative weightings in each geometry. The errors are variation bars, as described in Section 5.3.

B_{mean} (G)	Geometry	Energy ¹ (per cent)	Dipole ² (per cent)	Quad. ² (per cent)	Oct. ² (per cent)	Higher ² order (per cent)	Axi. ² (per cent)	Axi. ¹ (per cent)
HD 35296: 2007 data								
13.4 ^{+0.8} _{-0.4}	Poloidal	82 ⁺² ₋₁	20 ⁺¹ ₋₄	7 ⁺¹ ₋₁	12 ⁺⁰ ₋₂	61 ⁺⁴ ₋₁	7 ⁺⁷ ₋₂	6 ⁺⁵ ₋₂
	Toroidal	18 ⁺¹ ₂	33 ⁺¹ ₋₁₁	14 ⁺² ₋₁	5 ⁺³ ₋₀	48 ⁺⁹ ₋₂	72 ⁺¹ ₋₁₀	13 ⁺¹ ₋₂
HD 35296: 2008 data								
17.9 ^{+0.7} _{-1.3}	Poloidal	50 ⁺² ₋₃	7 ⁺¹ ₋₂	12 ⁺¹ ₋₁	8 ⁺² ₋₀	73 ⁺² ₋₄	13 ⁺³ ₋₃	7 ⁺¹ ₋₂
	Toroidal	50 ⁺³ ₋₂	53 ⁺⁶ ₋₁	6 ⁺⁴ ₋₁	3 ⁺¹ ₋₁	38 ⁺¹ ₋₉	76 ⁺⁵ ₋₀	38 ⁺⁴ ₋₁
HD 35296: 2008 data with reduced number of profiles to match the 2007 data set								
11.9 ^{+0.0} _{-1.0}	Poloidal	48 ⁺⁰ ₋₄	25 ⁺² ₋₄	16 ⁺⁹ ₋₀	16 ⁺⁰ ₋₆	43 ⁺² ₋₃	13 ⁺⁰ ₋₆	6 ⁺⁰ ₋₃
	Toroidal	52 ⁺⁴ ₋₀	71 ⁺⁸ ₋₂	12 ⁺⁴ ₋₄	4 ⁺¹ ₋₂	13 ⁺⁰ ₋₃	87 ⁺⁴ ₋₀	46 ⁺⁴ ₋₀
HD 29615: 2009 data								
81.6 ⁺²⁰ ₋₁₅	Poloidal	75 ⁺⁶ ₋₅	58 ⁺⁷ ₋₁₃	10 ⁺³ ₋₂	13 ⁺³ ₋₅	19 ⁺¹⁹ ₋₀	66 ⁺² ₋₁₂	49 ⁺⁶ ₋₁₀
	Toroidal	25 ⁺⁵ ₀	34 ⁺⁰ ₋₈	18 ⁺⁶ ₋₃	10 ⁺³ ₋₁	38 ⁺⁹ ₋₃	67 ⁺³ ₋₇	17 ⁺⁵ ₋₂

Notes. ¹This is a fraction (in per cent) of the total magnetic energy available.

²This is a fraction (in per cent) of the respective poloidal or toroidal field energy.

Listed also is the fraction of the poloidal or toroidal magnetic energy in the dipolar ($\ell = 1$), quadrupolar ($\ell = 2$), octupolar ($\ell = 3$) and higher order ($\ell \geq 4$) components as well as the fraction of energy stored in the axisymmetric component ($m = 0$).

stars. An alternative explanation may be offered by the work of Korhonen & Elstner (2011). Using dynamo calculations, they suggest that large starspots do not necessarily follow the actual differential rotation of the star, but have more solid-body-like behaviour, whereas the true surface differential rotation is only recovered if small magnetic features are added to the simulations. In addition, the paucity of low-level spot features could affect the differential rotation measurements. The differing measurements of differential rotation should be treated with caution until further Stokes I and V data are obtained for this star.

6.6 Surface differential rotation, rotation rate and convection zone depth

Barnes et al. (2005) showed a relationship between differential rotation ($\Delta\Omega$) and temperature, with increasing shear as a result of increasing temperature. Recent studies of G-dwarf stars such as HD 171488 (Marsden et al. 2006; Jeffers & Donati 2008; Jeffers et al. 2011) and HD 141943 (Marsden et al. 2011b) show significant levels of differential rotation beyond those observed by Barnes et al. (2005). HD 29615, like HD 171488, has extreme levels of rotational shear with a $\Delta\Omega = 0.48^{+0.11}_{-0.12}$ rad d⁻¹. HD 171488 has a 1.33 d rotation period with a $v\sin i = 38$ km s⁻¹ whereas HD 29615 has a rotational period of 2.34 d with a $v\sin i = 19.6$ km s⁻¹. Given that both HD 171488 and HD 29615 have similar photospheric temperatures and age, it appears that rotation rate has limited effect on rotational shear, thereby supporting the observations by Barnes et al. (2005).

Küker et al. (2011), using theoretical models, demonstrated that the extreme surface shear of stars such as HD 171488 (and by implications HD 29615) can only be explained with a shallow convection zone. HD 171488 has a convection zone depth (CZD) of $0.206 R_*$ ($0.233 R_{\odot}$; Jeffers et al. 2011) yet the CZD for HD 29615 was estimated to be $0.252 \pm 0.011 R_*$, as determined from the stellar evolution models of Siess et al. (2000). The estimate for HD 29615 was based on the $V - I$ colour index (van Leeuwen 2007) and the absolute magnitude, as determined from the maximum visual magnitude measured by the *Hipparcos* space mission. O’Neal, Saar &

Neff (1996) concluded that on some heavily spotted stars, the observed maximum V magnitude underestimates the brightness of the unspotted star by ~ 0.3 – 0.4 mag. For example, HD 106506 (Waite et al. 2011b) had a visual magnitude of ~ 8.54 but the unspotted magnitude was determined to be 8.38 (using the imaging code). As there was limited knowledge of the fractional spottedness of many of the stars that had their differential rotation already determined by other authors, it was decided to use the maximum visual magnitude listed in the *Hipparcos* data base with the caveat that this possibly leads to an overestimate of the true CZD. This measurement for HD 29615 places additional constraints on the conclusion of the theoretical work of Küker et al. (2011) that extreme levels of differential rotation require a shallow convection zone.

7 CONCLUSIONS

From the results presented in this paper, HD 35296 and HD 29615 are both Sun-like stars whose moderately rapid rotation has led to very complex surface magnetic fields that exhibit high levels of chromospheric activity and surface differential rotation. This variation in the chromospheric activity, with rotational phase, was evidenced by modulation of the Ca II H&K, Ca II IRT and H α spectral lines (HD 35296) and H α emission (HD 29615). High levels of differential rotation were measured. The differential rotation on HD 29615 showed a significant discrepancy in shear values between spot and magnetic features. This is an extreme example of a variation also observed for other lower mass stars. There are indications that the magnetic field of HD 35296 appears to have undergone a minor reorganization of its field from 2007 to 2008 thereby demonstrating the evolving nature of the magnetic topology on this star. We conclude that the dynamo operating on both of these stars is similar to that of other more active, rapidly rotating stars and is most likely a distributed dynamo operating throughout the convection zone.

ACKNOWLEDGEMENTS

Thanks must go to the staff of the TBL and the AAT in their assistance in taking these data. This work has only been possible

due to the brilliance of the late Meir Semel, from LESIA at Observatoire de Paris-Meudon. Sadly Meir passed away during 2012 but his memory and influence on spectropolarimetry will live on. The authors appreciate the time and dedication of the anonymous referee in producing constructive comments that has significantly improved this paper. This project has, in part, been supported by the Commonwealth of Australia under the International Science Linkages programme. SVJ and SBS acknowledge research funding by the Deutsche Forschungsgemeinschaft (DFG) under grant SFB 963/1 project A16. This project used the facilities of SIMBAD and *Hipparcos*. This research has made use of NASA's Astrophysics Data System.

REFERENCES

- Allende Prieto C., Lambert D. L., 1999, *A&A*, 352, 555
 Ammler-von Eiff M., Reiners A., 2012, *A&A*, 542, A116
 Aurière M., 2003, *EAS Publ. Ser.*, 9, 105
 Babcock H. W., 1961, *ApJ*, 133, 572
 Baliunas S. L. et al., 1985, *ApJ*, 294, 310
 Baliunas S. L. et al., 1995, *ApJ*, 438, 269
 Barnes J. R., Collier Cameron A., Donati J.-F., James D. J., Marsden S. C., Petit P., 2005, *MNRAS*, 357, L1
 Barry D. C., 1988, *ApJ*, 334, 436
 Berdyugina S. V., 2005, *Living Rev. Sol. Phys.*, 2, 8
 Bessell M. S., Castelli F., Plez B., 1998, *A&A*, 333, 231
 Brandenburg A., Krause F., Meinel R., Moss D., Tuominen I., 1989, *A&A*, 213, 411
 Brown S. F., Donati J.-F., Rees D. E., Semel M., 1991, *A&A*, 250, 463
 Brown B. P., Browning M. K., Brun A. S., Miesch M. S., Toomre J., 2010, *ApJ*, 711, 424
 Carter B. D., Brown S. F., Donati J.-F., Rees D. E., Semel M., 1996, *PASA*, 13, 150
 Casagrande L., Schönrich R., Asplund M., Cassisi S., Ramírez I., Meléndez J., Bensby T., Feltzing S., 2011, *A&A*, 530, A138
 Charbonneau P., MacGregor K. B., 1997, *ApJ*, 559, 1094
 Chen Y. Q., Nissen P. E., Benoni T., Zhao G., 2001, *A&A*, 371, 943
 Collier Cameron A., Donati J.-F., Semel M., 2002, *MNRAS*, 330, 699
 Dikpati M., Corbard T., Thompson M. J., Gilman P. A., 2002, *ApJ*, 575, L41
 Donahue R. A., 1993, PhD thesis, New Mexico State Univ.
 Donahue R. A., Baliunas S. L., 1992, *ApJ*, 393, L63
 Donahue R. A., Baliunas S. L., 1994, in Caillault J.-P., ed., *ASP Conf. Ser. Vol. 64, Cool Stars, Stellar Systems, and the Sun*. Astron. Soc. Pac., San Francisco, p. 396
 Donati J.-F., Brown S. F., 1997, *A&A*, 326, 1135
 Donati J.-F., Collier Cameron A., 1997, *MNRAS*, 291, 1
 Donati J.-F., Semel M., 1990, *Solar Phys.*, 128, 227
 Donati J.-F., Semel M., Carter B. D., Rees D. E., Collier Cameron A., 1997, *MNRAS*, 291, 658
 Donati J.-F. et al., 2003a, *MNRAS*, 345, 1145
 Donati J.-F., Collier Cameron A., Petit P., 2003b, *MNRAS*, 345, 1187
 Donati J.-F. et al., 2006, *MNRAS*, 370, 629
 Duncan D. K. et al., 1991, *ApJS*, 76, 383
 Dunstone N. J., Hussain G. A. J., Collier Cameron A., Marsden S. C., Jardine J., Barnes J. R., Ramírez Vèlez J. C., Donati J.-F., 2008, *MNRAS*, 387, 1525
 Farés R. et al., 2009, *MNRAS*, 398, 1383
 Gizis J. E., Reid I. N., Hawley S. L., 2002, *AJ*, 123, 3356
 Hall J. C., Henry G. W., Lockwood G. W., Skiff B. A., Saar S. H., 2009, *AJ*, 138, 312
 Holmberg J., Nordström B., Andersen J., 2009, *A&A*, 501, 941
 Jeffers S. V., Donati J.-F., 2008, *MNRAS*, 390, 635
 Jeffers S. V., Barnes J. R., Collier Cameron A., 2002, *MNRAS*, 331, 666
 Jeffers S. V., Donati J.-F., Alécian E., Marsden S. C., 2011, *MNRAS*, 411, 1301
 Kitchatinov L. L., Olemskoy S. V., 2011, *MNRAS*, 411, 1059
 Kochukhov O., Bagnulo S., Wade G. A., Sangalli L., Piskunov N., Landstreet J. D., Petit P., Sigut T. A. A., 2004, *MNRAS*, 414, 613
 Kochukhov O., Makaganiuk V., Piskunov N., 2010, *A&A*, 524, A5
 Korhonen H., Elstner D., 2011, *MNRAS*, 532, A106
 Küker M., Rüdiger G., Kitchatinov L. L., 2011, *A&A*, 530, A48
 Kurucz R. L., 1993, CDROM #13 (ATLAS9 atmospheric models) and CDROM #18 (ATLAS9 and SYNTHE routines, spectral line database)
 Lanza A. F., Rodonò M., Rosner R., 1998, *MNRAS*, 296, 893
 Li J. Z., Hu J. Y., 1998, *A&AS*, 132, 173
 MacGregor K. B., Charbonneau P., 1997, *ApJ*, 486, 484
 Marsden S. C., Waite I. A., Carter B. D., Donati J.-F., 2005, *MNRAS*, 359, 711
 Marsden S. C., Donati J.-F., Semel M., Petit P., Carter B. D., 2006, *MNRAS*, 370, 468
 Marsden S. C. et al., 2011a, *MNRAS*, 413, 1922
 Marsden S. C. et al., 2011b, *MNRAS*, 413, 1939
 Marsden S. C. et al., 2014, *MNRAS*, 444, 3517
 Messina S., Desidera S., Turatto M., Lanzafame A. C., Guinan E. F., 2010, *A&A*, 520, A15
 Montes D., López-Santiago J., Gálvez M. C., Fernández-Figueroa M. J., De Castro E., Cornide M., 2001, *MNRAS*, 328, 45
 Montes D., Crespo-Chacón I., Gálvez M. C., Fernández-Figueroa M. J., López-Santiago J., de Castro E., Cornide M., Hernán-Obispo J., 2004, in Ulla A., Manteiga M., eds, *Lecture Notes and Essays in Astrophysics I Real Sociedad Española de Física, Madrid*, p. 119
 Morgenthaler A. et al., 2012, *A&A*, 540, A138
 Moss D., Barker D. M., Brandenburg A., Tuominen I., 1995, *A&A*, 294, 155
 O'Neal D., Saar S. H., Neff J. E., 1996, *ApJ*, 463, 766
 Palacios A., Gebran M., Josselin E., Martins F., Plez B., Belmas M., Sanguillon M., Lèbre A., 2010, *A&A*, 516, A13
 Petit P., Donati J.-F., Collier Cameron A., 2002, *MNRAS*, 334, 374
 Petit P. et al., 2004a, *MNRAS*, 348, 1175
 Petit P. et al., 2004b, *MNRAS*, 351, 826
 Petit P. et al., 2008, *MNRAS*, 388, 80
 Petit P., Aurière M., Konstantinova-Antova R., Morgenthaler A., Perrin G., Roudier T., Donati J.-F., 2013, in Jean-Pierre R., Neiner C., eds, *Lecture Notes in Physics, Vol. 857, The Environments of the Sun and the Stars*. Springer-Verlag, Berlin, p. 231
 Reiners A., 2006, *A&A*, 446, 267
 Reiners A., Schmitt J. H. M. M., 2003a, *A&A*, 398, 647
 Reiners A., Schmitt J. H. M. M., 2003b, *A&A*, 412, 813
 Reinhold T., Reiners A., Basri G., 2013, *A&A*, 560, A4
 Rosén L., Kochukhov O., 2010, *A&A*, 548, A8
 Rutten R. G. M., 1984, *A&A*, 130, 353
 Samus N. N. et al., 2009, GCVS database, Version 2011 Jan. Institute of Astronomy of Russian Academy of Sciences and Sternberg State Astronomical Institute of the Moscow State University
 Semel M., 1989, *A&A*, 225, 456
 Semel M., Donati J.-F., Rees D. E., 1993, *A&A*, 278, 231
 Siess L., Dufour E., Forestini M., 2000, *A&A*, 358, 593
 Silvester J., Wade G. A., Kochukhov O., Bagnulo S., Folsom C. P., Hanes D., 2012, *MNRAS*, 426, 1003
 Sing K. D., 2010, *A&A*, 501, A21
 Skilling J., Bryan R. K., 1984, *MNRAS*, 211, 111
 Soderblom D. R., Stauffer J. R., Hudon J. D., Jones B. F., 1993a, *ApJS*, 85, 315
 Soderblom D. R., Pilachowski C. A., Fedele S. B., Jones B. F., 1993b, *AJ*, 105, 2299
 Takeda Y., Kawamoto S., 2005, *PASJ*, 57, 45
 Thatcher J. D., Robinson R. D., 1993, *MNRAS*, 262, 1
 Torres C. A. O., Quast G. R., da Silva L., de la Reza R., Melo C. H. F., Sterzik M., 2006, *A&A*, 460, 695
 Unruh Y. C., Collier Cameron A., 1995, *MNRAS*, 273, 1
 Unruh Y. C., Collier Cameron A., 1997, *MNRAS*, 290, L37
 van Leeuwen F., 2007, *A&A*, 474, 653

Wade G. A., Donati J.-F., Landstreet J. D., Shorlin S. L. S., 2000, MNRAS, 313, 823
Waite I. A., Marsden S. C., Carter B. D., Alécian E., Brown C., Burton D., Hart R., 2011a, PASA, 28, 323
Waite I. A., Marsden S. C., Carter B. D., Hart R., Donati J.-F., Ramirez Vèlez J. C., Semel M., Dunstone N., 2011b, MNRAS, 413, 1949

Wilson O. C., 1978, ApJ, 226, 397
Wright J. T., Marcy G. W., Butler P. R., Vogt S. S., 2004, ApJS, 152, 261
Zuckerman B., Song I., 2004, ARA&A, 42, 685

This paper has been typeset from a $\text{\TeX}/\text{\LaTeX}$ file prepared by the author.